101.1 (Glc-1), 129.4 (2C), 137.0 (2C), 139.1, 139.2, 169.5, 169.88, 169.93, 170.0, 170.4, 170.48, 170.53, 170.6, 170.7, 171.0. IR ($CHCl_3$) ν: 3020, 2928, 1753, 1682, 1514, 1464, 1429, 1367, 1251, 1138, 1069, 1040 cm^{-1}. HR-MS (FAB^+) *m/z*: 1340.4495 (Calcd for $C_{58}H_{87}NO_{25}SnNa$: 1340.4487).

8-(*p*-Tributylstannylphenyl)octyl 2-acetamido-3,4,6-tri-*O*-acetyl-2-deoxy-β-D-glucopyranosyl-(1→2)-3,4,6-tri-*O*-acetyl-α-D-mannopyranosyl-(1→6)-2,3,4-tri-*O*-acetyl-β-D-glucopyranoside (19b)

Potassium acetate (8.9 mg, 90.7 μmol), [1,1'-bis(diphenylphoshino)ferrocene]dichloropalladium(II) complex with CH_2Cl_2 (1:1) (2.5 mg, 3.1 μmol), and bis(tributyltin) (30 μL, 59.4 μmol) were added to a solution of **10b** (37.2 mg, 30.1 μmol) in NMP (1 mL). After stirring the reaction mixture for 2 h at room temperature, the mixture was extracted with EtOAc, washed with distilled water and a saturated aqueous solution of sodium chloride, successively, dried over sodium sulfate, and condensed *in vacuo*. The residue was purified by amine modified silica gel column chromatography (hexane : EtOAc = 1 : 1) to afford **19b** (12.9 mg, 31%). $[\alpha]_D$ +6.8° (*c* 0.80, $CHCl_3$). ^{1}H-NMR (C_5D_5N) δ: 0.87 (9H, t, *J* = 7.3 Hz), 1.11-1.15 (6H, m), 1.16-1.39 (8H, m), 1.35 (6H, sextet, *J* = 7.3 Hz), 1.51-1.71 (10H, m), 1.97, 1.99, 2.02, and 2.07 (each 3H, s), 2.09 (9H, s), 2.099, 2.103, and 2.11 (each 3H, s), 2.60 (2H, t, *J* = 7.9 Hz), 3.62 (1H, dt, *J* = 7.0, 9.5 Hz, $-OCH_2$), 3.76-3.79 (1H, m, Glc-6), 4.01 (1H, ddd, *J* = 2.2, 5.5, 10.1 Hz, GlcN-5), 4.04-4.16 (4H, m, GlcN-2, Glc-5, Glc-6, $-OCH_2$), 4.28 (1H, dd, *J* = 2.2, 12.3 Hz, GlcN-6), 4.38 (1H, ddd, *J* = 2.4, 5.1, 9.9 Hz, Man-5), 4.45 (1H, dd, *J* = 2.4, 12.1 Hz, Man-6), 4.53 (1H, dd, *J* = 5.1, 12.1 Hz, Man-6), 4.62 (1H, dd, *J* = 5.5, 12.3 Hz, GlcN-6), 4.79 (1H, dd, *J* = 1.5, 3.5 Hz, Man-2), 4.92 (1H, d, *J* = 8.1 Hz, Glc-1), 5.28 (1H, d, *J* = 1.5 Hz, Man-1), 5.41 (1H, t, *J* = 9.3 Hz, GlcN-4), 5.45 (1H, dd, *J* = 8.1, 9.7 Hz, Glc-2), 5.46 (1H, t, *J* = 9.5 Hz, Glc-4), 5.54 (1H, d, *J* = 8.4 Hz, GlcN-1), 5.61 (1H, dd, *J* = 3.5, 10.1 Hz, Man-3), 5.77 (1H, t, *J* = 9.7 Hz, Glc-3), 5.90 (1H, t, *J* = 10.1 Hz, Man-4), 6.04 (1H, dd, *J* = 9.3, 10.6 Hz, GlcN-3), 7.36 (1H, br d, *J* = 7.9 Hz), 7.63 (1H, br d, *J* = 7.9 Hz), 9.26 (1H, d, *J* = 8.1 Hz). ^{13}C-NMR (C_5D_5N) δ: 9.8 (3C), 13.9 (3C), 20.47, 20.49, 20.52, 20.7 (5C), 20.8, 23.2, 26.2, 27.6 (3C), 29.4 (3C), 29.55, 29.57, 29.78, 29.83, 31.9, 36.2, 55.7 (GlcN-2), 62.7 (GlcN-6), 63.0 (Man-6), 66.5 (Man-4), 67.2 (Glc-6), 69.6 (Man-5), 69.8 (GlcN-4), 70.1 (Glc-4), 70.3 ($-OCH_2$), 71.0 (Man-3), 72.16 (Glc-2), 72.21 (GlcN-5), 72.6 (GlcN-3), 72.9 (Glc-5), 73.6 (Glc-3), 74.5 (Man-2), 98.3 (Man-1), 99.7 (GlcN-1), 101.1 (Glc-1), 128.9 (2C), 137.0 (2C), 138.4, 143.1, 169.6, 169.87, 169.94, 170.0, 170.4, 170.48, 170.54, 170.6, 170.7, 171.0. IR ($CHCl_3$) ν: 3030, 2930, 2855, 1751, 1682, 1514, 1464, 1431, 1367, 1252, 1040 cm^{-1}. HR-MS (FAB^+) *m/z*: 1424.5430 (Calcd for $C_{64}H_{99}NO_{25}SnNa$: 1424.5426).

15-(*p*-Tributylstannylphenyl)pentadecyl 2-acetamido-3,4,6-tri-*O*-acetyl-2-deoxy-β-D-glucopyranosyl-(1→2)-3,4,6-tri-*O*-acetyl-α-D-manno- pyranosyl-(1→6)-2,3,4-tri-*O*-acetyl-β-D-glucopyranoside (19c)

Tetrakis(triphenylphosphine)palladium(0) (10.1 mg, 8.7 μmol), triphenylphosphine (2.3 mg, 8.8 μmol), and bis(tributyltin) (74 μL, 146.5 μmol) were added to a solution of **10c** (113.1 mg, 91.4 μmol) in toluene (2 mL). After stirring the reaction mixture for 5 h at 85 °C, the mixture was condensed *in vacuo*. The residue was purified by amine modified silica gel column chromatography (hexane: EtOAc = 1 : 1) to afford **19c** (7.7 mg, 16%). $[\alpha]_D$ −4.2° (*c* 1.36, $CHCl_3$). ^{1}H-NMR (C_5D_5N) δ: 0.87 (9H, t, *J* = 7.3 Hz), 1.11-1.15 (6H, m), 1.21-1.40 (30H, m), 1.54-1.70 (8H, m), 1.97, 1.99, 2.02, 2.07, 2.09, and 2.097 (each 3H, s), 2.101 (6H, s), 2.11 (6H, s), 2.62 (2H, t, *J* = 7.9 Hz), 3.64 (1H, dt, *J* = 6.8, 9.7 Hz, -OCH_2), 3.76-3.78 (1H, m, Glc-6), 4.01 (1H, ddd, *J* = 2.2, 5.5, 10.1 Hz, GlcN-5), 4.05-4.16 (4H, m, GlcN-2, Glc-5, Glc-6, -OCH_2), 4.28 (1H, dd, *J* = 2.2, 12.1 Hz, GlcN-6), 4.39 (1H, ddd, *J* = 2.4, 5.1, 10.3 Hz, Man-5), 4.45 (1H, dd, *J* = 2.4, 12.1 Hz, Man-6), 4.54 (1H, dd, *J* = 5.1, 12.1 Hz, Man-6), 4.62 (1H, dd, *J* = 5.5, 12.1 Hz, GlcN-6), 4.80 (1H, dd, *J* = 1.7, 3.5 Hz, Man-2), 4.93 (1H, d, *J* = 8.1 Hz, Glc-1), 5.28 (1H, d, *J* = 1.7 Hz, Man-1), 5.42 (1H, t, *J* = 9.3 Hz, GlcN-4), 5.45 (1H, dd, *J* = 8.1, 9.7 Hz, Glc-2), 5.46 (1H, t, *J* = 9.7 Hz, Glc-4), 5.54 (1H, d, *J* = 8.6 Hz, GlcN-1), 5.62 (1H, dd, *J* = 3.5, 10.3 Hz, Man-3), 5.77 (1H, t, *J* = 9.5 Hz, Glc-3), 5.90 (1H, t, *J* = 10.3 Hz, Man-4), 6.05 (1H, dd, *J* = 9.3, 10.6 Hz, GlcN-3), 7.38 (2H, br d, *J* = 7.9 Hz), 7.64 (2H, br d, *J* = 7.9 Hz), 9.26 (1H, d, *J* = 8.1 Hz). ^{13}C-NMR (C_5D_5N) δ: 9.8 (3C), 13.9 (3C), 20.47, 20.50, 20.52, 20.6 (2C), 20.7 (3C), 20.8, 23.2, 26.3, 27.6 (3C), 29.4 (3C), 29.5, 29.6, 29.7, 29.8, 29.88, 29.92, 29.98 (2C), 30.0 (3C), 31.9, 36.2, 55.7 (GlcN-2), 62.7 (GlcN-6), 63.0 (Man-6), 66.5 (Man-4), 67.2 (Glc-6), 69.6 (Man-5), 69.8 (GlcN-4), 70.1 (Glc-4), 70.3 (-OCH_2), 71.0 (Man-3), 72.17 (Glc-2), 72.22 (GlcN-5), 72.6 (GlcN-3), 72.9 (Glc-5), 73.6 (Glc-3), 74.5 (Man-2), 98.3 (Man-1), 99.7 (GlcN-1), 101.1 (Glc-1), 128.9 (2C), 137.0 (2C), 138.4, 143.2, 169.6, 169.9, 169.95, 169.97, 170.4, 170.48, 170.54, 170.6, 170.7, 171.0. IR ($CHCl_3$) ν: 3042, 2928, 2855, 1751, 1682, 1603, 1518, 1464, 1431, 1367, 1256, 1040 cm^{-1}. HR-MS (FAB$^+$) *m/z*: 1522.6519 (Calcd for $C_{71}H_{113}NO_{25}SnNa$: 1522.6521).

Radioiodinated 1a ([^{125}I]1a)

5% H_2O_2 aq. (10 μL), 0.1 M HCl aq. (10 μL), and [^{125}I]NaI (576 μCi) were added to a solution of tributyltin derivative **19a** (100 μg) in MeCN (20 μL). After stirring the reaction mixture at room temperature for 30 min, the mixture was added to a saturated aqueous solution of sodium thiosulfate, which was extracted with EtOAc and condensed *in vacuo*. The residue was treated with MeOH (20 μL) and sodium methoxide (28% in MeOH, 3 μL) for 30 min. The mixture was neutralized with 1 M hydrochloric acid. Purification of the residue on HPLC equipped with a Cosmosil 5C_{18} AR-300 column (4.6 × 150 mm, MeCN: H_2O = 20 : 80) with a flow rate of 1.0 mL/min afforded [^{125}I]**1a** (408 μCi), and its identity was identified by co-injection with **1a**. The radiochemical yield was 71% and the radiochemical purity was >99%.

Radioiodinated 1b ([^{125}I]1b)

5% H_2O_2 aq. (10 μL), 0.1 M HCl aq. (10 μL), and [^{125}I]NaI (400 μCi) were added to a solution of tributyltin derivative **19b** (100 μg) in MeCN (20 μL). After stirring the reaction mixture at room temperature for 30 min, the mixture was added to a saturated aqueous solution of sodium thiosulafte, which was extracted with EtOAc and condensed *in vacuo*. The residue was treated with MeOH (20 μL) and sodium methoxide (28% in MeOH, 3 μL) for 30 min. The mixture was neutralized with 1 M hydrochloric acid. Purification of the residue on HPLC equipped with a Cosmosil $5C_{18}$ AR-300 column (4.6 × 150 mm, MeCN : H_2O = 40 : 60) with a flow rate of 1.0 mL/min afforded [^{125}I]**1b** (304 μCi), and its identity was identified by co-injection with **1b**. The radiochemical yield was 76% and the radiochemical purity was >99%.

Radioiodinated 1c ([^{125}I]1c)

5% H_2O_2 aq. (10 μL), 0.1 M HCl aq. (10 μL), and [^{125}I]NaI (600 μCi) were added to a solution of tributyltin derivative **19c** (100 μg) in MeCN (20 μL). After stirring the reaction mixture at room temperature for 30 min, the mixture was added to a saturated aqueous solution of sodium thiosulafte, which was extracted with EtOAc and condensed *in vacuo*. The residue was treated with MeOH (20 μL) and sodium methoxide (28% in MeOH, 3 μL) for 30 min. The mixture was neutralized with 1 M hydrochloric acid. Purification of the residue on HPLC equipped with a Cosmosil $5C_{18}$ AR-300 column (4.6 × 150 mm, MeCN : H_2O = 60 : 40) with a flow rate of 1.0 mL/min afforded [^{125}I]**1c** (326 μCi), and its identity was identified by co-injection with **1c**. The radiochemical yield was 54% and the radiochemical purity was >99%.

REFERENCES AND NOTE

1. R. D. Cummings, I. S. Trowbridge, and S. Kornfeld, *J. Biol. Chem.*, 1982, **257**, 13421.
2. K. Yamashita, Y. Tachibana, T. Ohkura, and A. Kobata, *J. Biol. Chem.*, 1985, **260**, 3963.
3. M. Pierce and J. Arango, *J. Biol. Chem.*, 1986, **261**, 10772.
4. J. W. Dennis, S. Laferte, C. Waghorne, M. L. Breitman, and R. S. Kerbel, *Science*, 1987, **236**, 582.
5. J. W. Dennis and S. Laferte, *Cancer Res.*, 1989, **49**, 945.
6. B. Fernandes, U. Sagman, M. Auger, M. Demetrio, and J. W. Dennis, *Cancer Res.*, 1991, **51**, 718.
7. E. Miyoshi, A. Nishikawa, Y. Ihara, J. Gu, T. Sugiyama, N. Hayashi, H. Fusamoto, T. Kamada, and N. Taniguchi, *Cancer Res.*, 1993, **53**, 3899.
8. K. Murata, E. Miyoshi, M. Kameyama, O. Ishikawa, T. Kabuto, Y. Sasaki, M. Hiratsuka, H. Ohigashi, S. Ishiguro, S. Ito, H. Honda, F. Takemura, N. Taniguchi, and S. Imaoka, *Clin. Cancer*

Res., 2000, **6**, 1772.

9. J. W. Dennis, J. Pawling, P. Cheung, E. Partridge, and M. Demetriou, *Biochim. Biophys. Acta*, 2002, **157**, 414.
10. T. Saito, E. Miyoshi, K. Sasai, N. Nakano, H. Eguchi, K. Honke, and N. Taniguchi, *J. Biol. Chem.*, 2002, **277**, 17002.
11. T. Mukai, M. Hagimori, K. Arimitsu, T. Katoh, M. Ukon, T. Kajimoto, H. Kimura, Y. Magata, E. Miyoshi, N. Taniguchi, M. Node, and H. Saji, *Bioorg. Med. Chem.*, 2011, **19**, 4312.
12. T. Kajimoto, Y. Ishioka, T. Katoh, and M. Node, *Bioorg. Med. Chem. Lett.*, 2006, **16**, 5736.
13. T. Kajimoto, Y. Ishioka, T. Katoh, and M. Node, *J. Carbohydr. Chem.*, 2007, **26**, 469.
14. T. Kajimoto, K. Arimitsu, M. Ozeki, and M. Node, *Chem. Pharm. Bull.*, 2010, **58**, 758.
15. Hydrogenolysis of **14** or **15** with Pd/C or $Pd(OH)_2/C$ did not proceed.
16. T. L. Ho and G. A. Olah, *Angew. Chem., Int. Ed. Engl.*, 1976, **15**, 774, See also, M. E. Jung and M. A. Lyster, *J. Am. Chem. Soc.*, 1977, **99**, 968.
17. A. N. Pinchuk, M. A. Rampy, M. A. Longino, R. W. Scott Skinner, M. D. Gross, J. P. Weichert, and R. E. Counsell, *J. Med. Chem.*, 2006, **49**, 2155.
18. Y. Hayakawa, H. Kato, M. Uchiyama, H. Kajino, and R. Noyori, *J. Org. Chem.*, 1986, **51**, 2400.
19. A. Hasegawa, T. Nagahama, H. Ohki, K. Hotta, H. Ishida, and M. Kiso, *J. Carbohydr. Chem.*, 1991, **10**, 493.
20. M. E. Mahoney, A. Oliver, O. Einarsdottir, and J. P. Konopelski, *J. Org. Chem.*, 2009, **74**, 8212.
21. W. Qu, K. Ploessl, H. Truong, M-P. Kung, and H. K. Kung, *Bioorg. Med. Chem. Lett.*, 2009, **19**, 3382.

Hindawi Publishing Corporation
International Journal of Molecular Imaging
Volume 2011, Article ID 537687, 7 pages
doi:10.1155/2011/537687

Review Article

Advances in Drug Design of Radiometal-Based Imaging Agents for Bone Disorders

Kazuma Ogawa[1] and Hideo Saji[2]

[1] *Division of Pharmaceutical Sciences, Graduate School of Natural Science and Technology, Kanazawa University, Kakuma-machi, Kanazawa 920-1192, Japan*
[2] *Department of Patho-Functional Bioanalysis, Graduate School of Pharmaceutical Sciences, Kyoto University, Kyoto 606-8501, Japan*

Correspondence should be addressed to Kazuma Ogawa, kogawa@p.kanazawa-u.ac.jp

Received 5 August 2011; Accepted 26 September 2011

Academic Editor: Habib Zaidi

Nuclear medicine bone imaging has been the optimum diagnosis for the detection of bone disorders because the lesion could be detectable before the appearance of symptomatic and radiographic changes. Over the past three decades, ^{99m}Tc-MDP and ^{99m}Tc-HMDP have been used as bone scintigraphic agents because of their superior biodistribution characteristics, although they are far from optimal from a chemical and pharmaceutical point of view. Recently, a more logical drug design has been proposed as a concept of bifunctional radiopharmaceuticals in which the carrier molecules (bisphosphonates) and radiometal chelating groups are separated within a molecule, specifically, ^{99m}Tc-mononuclear complex-conjugated bisphosphonate. Some of the ^{99m}Tc-mononuclear complex-conjugated bisphosphonate compounds showed superior biodistribution in preclinical studies. Moreover, the drug design concept could be applied to ^{68}Ga PET bone imaging agents. These studies would provide useful information for the development of radiometal-based imaging and therapeutic agents for bone disorders such as bone metastases.

1. Background

The skeleton is one of the most common organs to be affected by metastatic cancer. Carcinomas of the breast, lung, prostate, kidney, and thyroid have a tendency to easily metastasize to bone [1]. Although there has been significant advancement in imaging technologies, such as CT and MR, nuclear medicine bone imaging has been the optimum diagnosis for the detection of bone disorders, such as bone metastases, because of its high sensitivity. Namely, bone-seeking radiopharmaceuticals usually localize in skeletal lesions before the appearance of symptomatic and radiographic changes and the resulting easy evaluation of the entire skeleton [2]. This paper reviews currently available ^{99m}Tc radiopharmaceuticals for bone scintigraphy and advances in drug design of radiometal-based bone-targeted compounds.

2. ^{99m}Tc-Bisphosphonate Complexes

Although some radiometals, such as lanthanide and rare earth, localize in bone by themselves, pertechnetate ($^{99m}TcO_4^-$) hardly accumulates in bone by itself. Accordingly, a carrier for bone is necessary in order to take bone images with technetium. The first bone-seeking ^{99m}Tc compound, a complex of reduced ^{99m}Tc and sodium tripolyphosphate, was reported in 1971 [3], followed by a long-chain linear polyphosphate [4] and pyrophosphate [5]. Pyrophosphate (Figure 1(a)) is composed of only two phosphate moieties and is the simplest polyphosphate. ^{99m}Tc-pyrophosphate is now seldom used for skeletal imaging because of its high soft tissue background activity but is still employed to determine myocardial infarction. Unfortunately, pyrophosphate and polyphosphate are susceptible to *in vivo* degradation by enzymes such as alkaline phosphatases, resulting in the release of free technetium from the complexes. Subsequently, three groups almost simultaneously reported the ^{99m}Tc complex of 1-hydroxyethyliden-1,1-diphosphonate (HEDP, Figure 1(b)) as a new bone imaging agent [6–8]. HEDP is one of the bisphosphonate (diphosphonate) compounds, which are known as compounds with high affinity for bone and inhibitors of bone resorption. Bisphosphonate compounds were synthesized with a P–C–P bonding

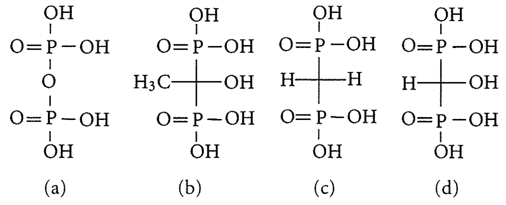

Figure 1: Chemical structures of bisphosphonates analogs (a) pyrophosphate, (b) HEDP, (c) MDP, and (d) HMDP.

sequence instead of the P–O–P sequence of pyrophosphate. Although these two chemical structures are similar, the P–C–P bond angles are smaller (117 degrees) than the P–O–P bond angles (128.7 degrees) and the P–C interatomic distance (1.79 Å) is longer than that of P–O (1.63 Å) [9]. Bisphosphonate bonding is very stable chemically and affords greater resistance to *in vivo* phosphatase hydrolysis. As a result, ^{99m}Tc-HEDP exhibited more rapid clearance from blood and higher uptake in bone. In clinical study, ^{99m}Tc-HEDP showed significantly higher lesion-to-normal bone ratios when compared with either ^{99m}Tc-pyrophosphate or ^{99m}Tc-polyphosphate [10].

After introduction of ^{99m}Tc-methylene diphosphonate (MDP, Figure 1(c)) by Subramanian et al. [11] in 1975 and ^{99m}Tc-hydroxymethylene diphosphonate (HMDP, Figure 1(d)) by Bevan et al. [12] in 1980, ^{99m}Tc-MDP, and ^{99m}Tc-HMDP, which showed superior biodistribution compared to ^{99m}Tc-HEDP, have been used as radiopharmaceuticals for bone scintigraphy for over thirty years [13–15]. ^{99m}Tc-MDP is postulated to form a bidentate-bidentate bridge with hydroxyapatite while the presence of the hydroxyl group in ^{99m}Tc-HMDP would convert the ligand to form a bidentate-tridentate bridge and is expected to enhance the hydroxyapatite affinity of the ^{99m}Tc complex [12, 16]. However, the lower bone accumulation of ^{99m}Tc-HEDP is not well understood because ^{99m}Tc-HEDP should also form bidentate-tridentate binding. Increasing steric hindrance associated with the methyl group at the central carbon atom of HEDP, the difference in solubility, and differences in molecular size as well as in the bisphosphonate polymeric complexes themselves have all been suggested [12, 17].

The accumulation of ^{99m}Tc-bisphoshonate complexes in bone must be derived from the coordination of bisphosphonate to calcium in the hydroxyapatite of bone, but the mechanism of high uptake to lesion sites in bone has not been completely elucidated. One factor should be the increased vascularity and regional distribution of blood flow that results from disease. However, it has been shown that regional bone blood flow alone does not account for the increased uptake of radiopharmaceuticals [18]. Other factors are involved in their binding and interaction with bone. It is generally assumed that ^{99m}Tc-bisphoshonate complexes accumulate at sites of active bone metabolism, that is to say, at areas of new bone formation or calcification [19, 20]. It has also been reported that the accumulation mechanisms might be both adsorption onto the surface of hydroxyapatite in bone and incorporation into the crystalline structure of hydroxyapatite [21]. Newly formed bone has a much larger surface area than does stable bone. That is, the crystalline structure of hydroxyapatite in newly formed bone is amorphous and has a greater surface area than that in normal bone [22]. An *in vitro* study demonstrated that bisphosphonate compounds have significantly higher adsorption on amorphous calcium phosphate than on crystalline calcium phosphate [17].

Bisphosphonate compounds form multiple complexes with reduced ^{99m}Tc. By using high-performance liquid chromatography (HPLC), the relative composition of ^{99m}Tc-bisphosphonate complexes in a reaction mixture has been found to vary with pH and with technetium, and with oxygen concentrations [23]. It has been postulated that ^{99m}Tc-bisphosphonate complexes would be a mixture of monomers, oxo-bridged dimers, and oligomeric clusters with varying technetium-oxo core configurations, oxidation states, and ligand coordination numbers [24]. These radiolabeled species have different biodistribution properties. It was reported that the smallest, low-charged, mononuclear ^{99m}Tc-bisphosphonate complex has the greatest uptake in bone lesions and the highest lesion-to-muscle and lesion-to-normal bone ratios in experiments using each isolated complex by HPLC [25]. Thus, the exact structures and mechanisms of the action of ^{99m}Tc-labeled bisphosphonate remain uncertain.

3. New Drug Design Concept of ^{99m}Tc-Labeled Bisphosphonate (^{99m}Tc Complex-Conjugated Bisphosphonate Compounds)

As mentioned above, despite over three decades of clinical use of ^{99m}Tc-bisphosphonate complexes, these radiopharmaceuticals are far from optimal from a chemical and pharmaceutical point of view. For example, their structures and compositions remain unknown because they cannot be obtained as a well-defined single-chemical species, but as mixtures of short-chain and long-chain oligomers. The biological behavior of this type of tracer is also affected by the different degrees of ionization and by variations in the relative amount of oligomers after preparation [23].

In addition, in clinical studies, an interval of 2 to 6 hours is required between an injection of ^{99m}Tc-labeled bisphosphonates and obtaining bone images [15]. Shortening this interval would lessen the burden to patients in terms of total examination length and radiation dose absorbed. To enable imaging at an earlier time after injection, a radiopharmaceutical with higher affinity for bone might be advantageous. Although the accumulation of bisphosphonate compounds in bone is achieved by binding the phosphonate groups with the Ca^{2+} of hydroxyapatite crystals [26], the phosphonate groups in ^{99m}Tc-MDP and ^{99m}Tc-HMDP serve as both coordinating ligands and Ca^{2+} binding functional groups [27], which might decrease the inherent accumulation of MDP and HMDP in bone.

Recently, to improve the ^{99m}Tc-labeled bisphosphonates currently used, a more logical drug design has been proposed based on the concept of bifunctional radiopharmaceuticals in which the carrier molecules (bisphosphonate) and radiometal chelating groups are separated within the molecule

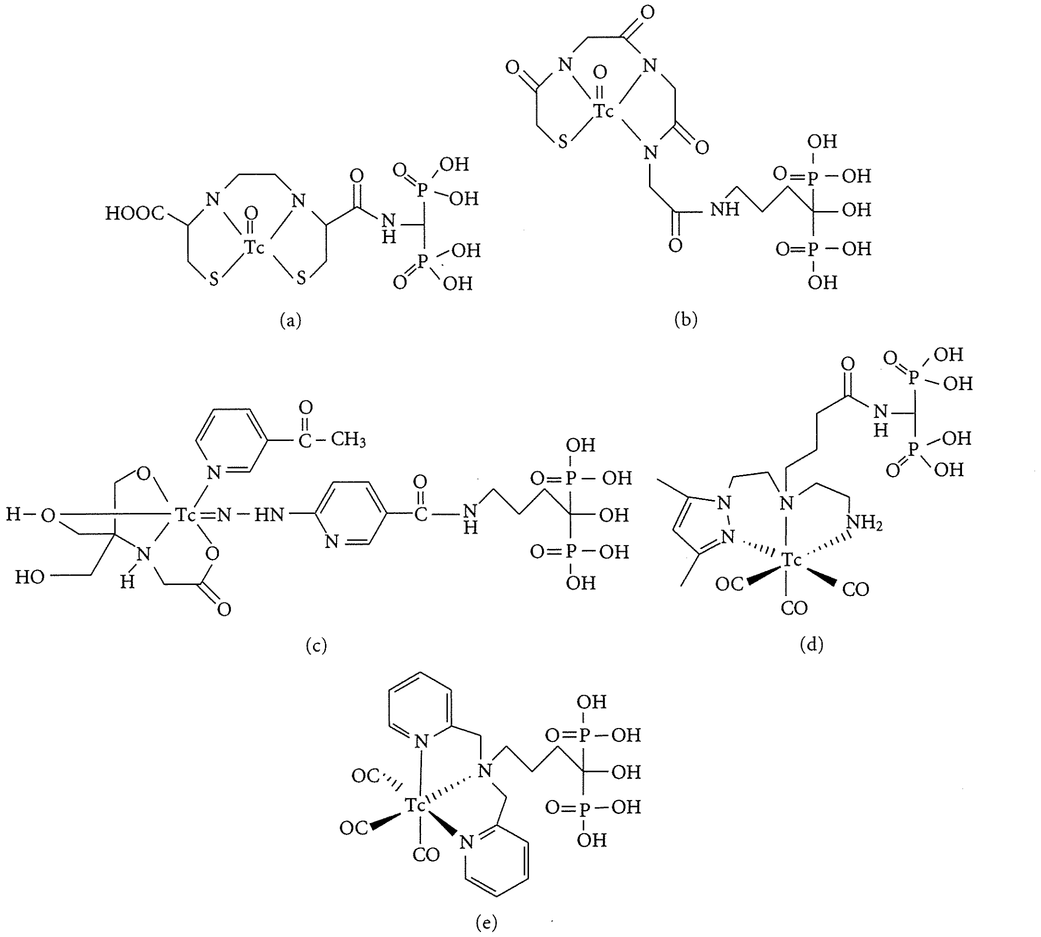

Figure 2: Chemical structures of Tc-complex-conjugated bisphosphonate compounds (a) Tc-ECAMDP, (b) Tc-MAG3-HBP, (c) Tc-HYNIC-HBP, (d) $Tc(CO)_3(\kappa^3\text{-pz-BPOH})]^+$, and (e) $Tc(CO)_3$-DPA-alendronate.

so that they can each function independently and effectively. In particular, ^{99m}Tc-mononuclear complex-conjugated bisphosphonate compounds have been reported [28–31]. It was hypothesized that the bone affinity of ^{99m}Tc labeled bisphosphonate would be enhanced by conjugating a stable mononuclear ^{99m}Tc chelating group with a bisphosphonate moiety so that the conjugation does not impair the inherent chemical and biological properties of the bisphosphonate compounds. ^{99m}Tc-L,L-ethylene dicysteine (EC), ^{99m}Tc-mercaptoacetylglycylglycylglycine (MAG3), ^{99m}Tc-6-hydrazinonicotinic acid (HYNIC), ^{99m}Tc-tricarbonyl anchored by pyrazolyl- (pz-) containing ligand, and ^{99m}Tc-tricarbonyl dipicolylamine (DPA) were selected as ^{99m}Tc chelating molecules, and were conjugated with bisphosphonate compounds, (^{99m}Tc-ECAMDP, ^{99m}Tc-MAG3-HBP, ^{99m}Tc-HYNIC-HBP, $[^{99m}Tc(CO)_3(\kappa^3\text{-pz-BPOH})]^+$, and $^{99m}Tc(CO)_3$-DPA-alendronate, resp., Figure 2).

In the drug design of the ^{99m}Tc-mononuclear complex-conjugated bisphosphonate compounds, since these ligands contain a bisphosphonate site, there is a possibility that ^{99m}Tc coordinates not with the proposed metal coordination moiety, such as EC, MAG3, and HYNIC but with the bisphosphonate moiety. To ascertain whether ^{99m}Tc is chelated with only the proposed metal coordination moiety, some experiments were performed. For example, in the case of ^{99m}Tc-HYNIC-HBP, ^{99m}Tc-HYNIC-HBP was also prepared by the coupling of ^{99m}Tc-HYNIC previously complexed with the bisphosphonate site (prelabel method). RP-HPLC analysis revealed the ^{99m}Tc-HYNIC-HBP by the prelabel method to be identical to that obtained from the labeling of HYNIC-HBP with ^{99m}Tc. These findings exclude the possibility of complexation between technetium and the bisphosphonate structure, and indicate the chelation of ^{99m}Tc with the HYNIC moiety in HYNIC-HBP.

In these new compounds, ^{99m}Tc-MAG3-HBP, ^{99m}Tc-HYNIC-HBP, and $^{99m}Tc(CO)_3$-DPA-alendronate were investigated for *in vitro* hydroxyapatite binding as an index of bone affinity. ^{99m}Tc-MAG3-HBP and ^{99m}Tc-HYNIC-HBP showed a significantly higher rate of binding to hydroxyapatite than did ^{99m}Tc-HMDP. $^{99m}Tc(CO)_3$-DPA-alendronate showed a higher affinity to hydroxyapatite than did ^{99m}Tc-MDP. At the same time, all new ^{99m}Tc-mononuclear

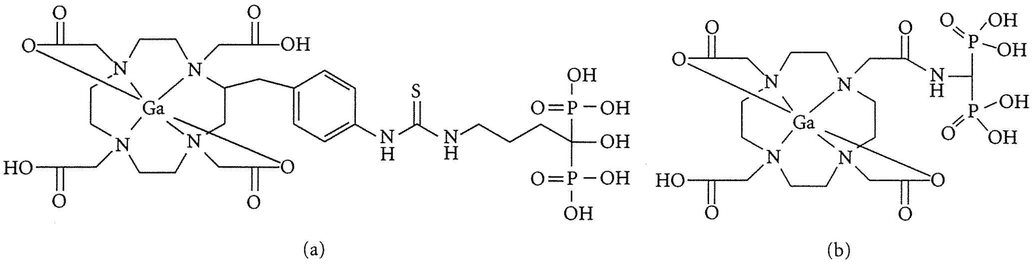

Figure 3: Chemical structures of radiogallium complex-conjugated bisphosphonate compounds (a) Ga-DOTA-Bn-SCN-HBP and (b) Ga-BPAMD.

complex-conjugated bisphosphonate compounds exhibited high bone uptake in *in vivo* animal experiments. ^{99m}Tc-EC-AMDP and ^{99m}Tc-HYNIC-HBP showed especially superior results; ^{99m}Tc-EC-AMDP and ^{99m}Tc-HYNIC-HBP showed significantly higher bone-to-blood ratios of radioactivity than did ^{99m}Tc-MDP and ^{99m}Tc-HMDP.

4. Radiogallium-Labeled Compounds as Bone Imaging Agents for PET

^{68}Ga is one of the greatest practical and interesting radionuclides for clinical positron emission tomography (PET) because of its radiophysical properties ($T_{1/2}$ = 68 min) [32]. ^{68}Ga is a generator-produced nuclide and can be eluted at any time on demand. Specifically, it does not require an on-site cyclotron. In principle, the long half-life of the parent nuclide ^{68}Ge ($T_{1/2}$ = 270.8 days) provides a long life-span generator.

Investigations of ^{68}Ga-labeled compounds for bone imaging were previously reported in the 1970s [33, 34]. In these reports, gallium was labeled with tripolyphosphate or ethylenediamine tetramethylene phosphonate (EDTMP) or diethylenetriamine pentamethylene phosphonate (DTPMP). These complexes showed high uptakes in bone. However, since use of the PET camera generally did not spread in the 1970s and the quality of PET cameras was not high, the attention given to ^{68}Ga PET imaging agents was not so high.

For the last decade, ^{68}Ga as a nuclide has been considered a useful radionuclide for PET imaging. Thus, many ^{68}Ga-labeled compounds have been developed. Recently, ^{68}Ga-EDTMP was also reevaluated by Mitterhauser et al. [35]. However, they stated that the advantage of ^{68}Ga-EDTMP over [^{18}F]-fluoride was not apparent and that the future clinical prospect of ^{68}Ga-EDTMP remained speculative.

The above-mentioned drug concept of stable mononuclear complex-conjugated bisphosphonate could be applicable to not only technetium complex radiopharmaceuticals but also to gallium radiopharmaceuticals. To develop a new PET tracer with radiogallium for imaging bone disorders such as bone metastases, 1,4,7,10-tetraazacyclododecane-1,4,7,10-tetraacetic acid (DOTA) was chosen as a chelating site because it has been well known that Ga forms a stable complex with DOTA. Therefore, Ga-DOTA-conjugated bisphosphonate compounds (^{67}Ga-DOTA-Bn-SCN-HBP and ^{68}Ga-BPAMD, Figure 3) have been developed [36, 37]. Actually, in biodistribution experiments, ^{67}Ga-DOTA-Bn-SCN-HBP rapidly accumulated in bone but was rarely observed in tissues other than bone. In addition, PET/CT imaging of bone metastases with ^{68}Ga-BPAMD showed high uptake in osteoblastic metastases of human (Figure 4). The maximal standardized uptake was 77.1 and 62.1 in the 10th thoracic and L2 vertebra versus 39.1 and 39.2 for ^{18}F-fluoride PET, respectively. These results suggest that the drug design concept of radiogallium complex-conjugated bisphosphonate could be useful for the development of ^{68}Ga PET imaging agents for bone disorders such as bone metastases.

5. ^{18}F-Fluoride as Bone Imaging Agent for PET

^{18}F-fluoride was initially reported by Blau et al. in 1962 [38]. After the development of ^{99m}Tc-labeled bone scintigraphy agents, such as ^{99m}Tc-MDP, ^{18}F-fluoride was replaced by them because the physical characteristics of ^{99m}Tc were more convenient for imaging with conventional gamma cameras in those days. However, in the last decade, PET and PET/CT have evolved significantly and become widespread. The situation has similarly changed for ^{68}Ga-labeled compounds. The changes caused the reemergence of ^{18}F-fluoride bone imaging with PET because current PET cameras have higher spatial resolution and greater sensitivity than conventional gamma cameras.

Like ^{99m}Tc-MDP as mentioned above, it is known that the distribution of ^{18}F-fluoride in bone also reflects both blood flow in bone and osteoblastic activity. Once ^{18}F-fluoride reaches the surface of the newly formed hydroxyapatite crystals, fluoride anions are isomorphously exchanged with the hydroxyl group in hydroxyapatite ($Ca_{10}(PO_4)_6(OH)_2$) and fluorapatite ($Ca_{10}(PO_4)_6F_2$) is formed [39]. A previous paper reported that electron probe X-ray fluorescence studies on the topographical distribution of fluoride at the microscopic level in the iliac bone of an osteoporotic patient being treated with fluoride [40]. The results indicate that the distribution of ^{18}F-fluoride in newly mineralized bone is similar to that of ^{99m}Tc-MDP.

There is an important difference between ^{18}F-fluoride and ^{99m}Tc-MDP in terms of their protein binding rates. ^{18}F-fluoride barely binds to serum protein [41] whereas ^{99m}Tc-MDP shows significant protein bindings. The difference in protein binding causes a difference in blood clearance between ^{18}F-fluoride and ^{99m}Tc-MDP. Hence, an interval of 2-3 hours is needed between an injection of ^{99m}Tc-MDP and bone imaging. In contrast, bone imaging can be performed less than 1 hour after an injection of ^{18}F-fluoride. Another

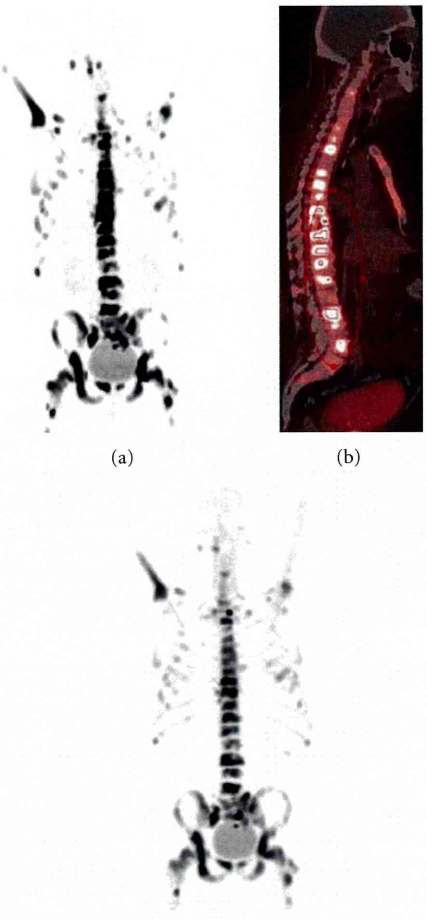

Figure 4: ^{68}Ga-BPAMD was injected i.v. into a patient with known extensive bone metastases of prostate cancer. ^{68}Ga-BPAMD (maximum intensity projection (MIP) 50 min after injection (p.i.), 462 MBq) revealed intense accumulation in multiple osteoblastic lesions in the central skeleton, ribs, and proximal extremities: (a) = coronal PET, (b) = sagittal PET/CT. For comparison, (c) shows ^{18}F-fluoride PET (sagittal, MIP 90 min p.i., 270 MBq). With kind permission from Springer Science + Business Media: [36].

difference between ^{18}F-fluoride and ^{99m}Tc-MDP is in terms of uptake to blood cells. ^{18}F-fluoride is taken up by red blood cells. The erythrocyte concentration of ^{18}F-fluoride is approximately 45–50% of the plasma concentration, namely, approximately 30% of total blood concentration. However, ^{18}F-fluoride is freely diffusible from red blood cells to the bone surface, so the uptake of ^{18}F-fluoride to red blood cells should not interfere with the accumulation of ^{18}F-fluoride in bone [41].

In clinical use in oncology, some papers reported on a comparison between ^{18}F-fluoride PET and planar ^{99m}Tc-MDP scintigraphy in the detection of bone metastases [42, 43]. ^{18}F-fluoride PET was more sensitive in detecting bone metastases than planar ^{99m}Tc-MDP scintigraphy. However, the cause of increased sensitivity—whether it was derived from ^{18}F-fluoride itself as a tracer or because of the improved performance of the PET camera—could not be determined.

Specifically, ^{18}F-fluoride PET has two important advantages in diagnosis imaging over planar ^{99m}Tc-MDP scintigraphy: superior sensitivity and a shorter interval between injection of a tracer and bone imaging. Thus, the use of ^{18}F-fluoride could become common in the future.

6. Conclusion

Over the past three decades, ^{99m}Tc-MDP and ^{99m}Tc-HMDP have been used for detecting bone metastases, although their mechanisms of accumulation remain uncertain. Recent efforts of chelate-conjugated bisphosphonates and their derivatives have provided chemically well-characterized new ^{99m}Tc-labeled bone-seeking tracers. Furthermore, the drug design concept could be applied to ^{68}Ga PET bone imaging agents. These studies would provide useful information for the development of radiometal-based imaging and therapeutic agents for bone disorders such as bone metastases.

References

[1] R. E. Coleman, "Skeletal complications of malignancy," *Cancer*, vol. 80, no. 8, pp. 1588–1594, 1997.

[2] A. Z. Krasnow, R. S. Hellman, M. E. Timins, B. D. Collier, T. Anderson, and A. T. Isitman, "Diagnostic bone scanning in oncology," *Seminars in Nuclear Medicine*, vol. 27, no. 2, pp. 107–141, 1997.

[3] G. Subramanian and J. G. McAfee, "A new complex of ^{99m}Tc for skeletal imaging," *Radiology*, vol. 99, no. 1, pp. 192–196, 1971.

[4] G. Subramanian, J. G. McAfee, E. G. Bell, R. J. Blair, R. E. O'Mara, and P. H. Ralston, "^{99m}Tc-labeled polyphosphate as a skeletal imaging agent," *Radiology*, vol. 102, no. 3, pp. 701–704, 1972.

[5] J. W. Fletcher, E. Solaric George, R. E. Henry, and R. M. Donati, "Evaluation of ^{99m}Tc pyrophosphate as a bone imaging agent," *Radiology*, vol. 109, no. 2, pp. 467–469, 1973.

[6] G. Subramanian, J. G. McAfee, R. J. Blair, A. Mehter, and T. Connor, "^{99m}Tc-EHDP: a potential radiopharmaceutical for skeletal imaging," *Journal of Nuclear Medicine*, vol. 13, no. 12, pp. 947–950, 1972.

[7] F. P. Castronovo and R. J. Callahan, "New bone scanning agent: ^{99m}Tc-labeled 1-hydroxy-ethylidene-1, 1-disodium phosphonate," *Journal of Nuclear Medicine*, vol. 13, no. 11, pp. 823–827, 1972.

[8] Y. Yano, J. McRae, D. C. Van Dyke, and H. O. Anger, "Technetium-99m-labeled stannous ethane-1-hydroxy-1 1-diphosphonate: a new bone scanning agent," *Journal of Nuclear Medicine*, vol. 14, no. 2, pp. 73–78, 1973.

[9] M. Larsen, R. Willett, and R. G. Yount, "Imidodiphosphate and pyrophosphate: possible biological significance of similar structures," *Science*, vol. 166, no. 3912, pp. 1510–1511, 1969.

[10] D. L. Citrin, R. G. Bessent, J. B. Tuohy et al., "A comparison of phosphate bone-scanning agents in normal subjects and patients with malignant disease," *The British Journal of Radiology*, vol. 48, pp. 118–121, 1975.

[11] G. Subramanian, J. G. McAfee, and R. J. Blair, "Technetium 99m methylene diphosphonate: a superior agent for skeletal

imaging: comparison with other technetium complexes," *Journal of Nuclear Medicine*, vol. 16, no. 8, pp. 744–755, 1975.

[12] J. A. Bevan, A. J. Tofe, and J. J. Benedict, "Tc-99m HMDP (hydroxymethylene diphosphonate): a radiopharmaceutical for skeletal and acute myocardial infarct imaging. I. Synthesis and distribution in animals," *Journal of Nuclear Medicine*, vol. 21, no. 10, pp. 961–966, 1980.

[13] P. A. Domstad, J. J. Coupal, E. E. Kim, J. S. Blake, and F. H. DeLand, "^{99m}Tc-hydroxymethane diphosphonate: a new bone imaging agent with a low tin content," *Radiology*, vol. 136, pp. 209–211, 1980.

[14] C. Mari, A. Catafau, and I. Carrio, "Bone scintigraphy and metabolic disorders," *Quarterly Journal of Nuclear Medicine*, vol. 43, no. 3, pp. 259–267, 1999.

[15] C. Love, A. S. Din, M. B. Tomas, T. P. Kalapparambath, and C. J. Palestro, "Radionuclide bone imaging: an illustrative review," *Radiographics*, vol. 23, no. 2, pp. 341–358, 2003.

[16] S. S. Jurisson, J. J. Benedict, R. C. Elder, R. Whittle, and E. Deutsch, "Calcium affinity of coordinated diphosphonate ligands. Single-crystal structure of $[(en)_2Co(O_2P(OH)CH_2P(OH)O_2)]ClO_4 \cdot H_2O$. Implications for the chemistry of technetium-99m-diphosphonate skeletal imaging agents," *Inorganic Chemistry*, vol. 22, no. 9, pp. 1332–1338, 1983.

[17] M. D. Francis, D. L. Ferguson, and A. J. Tofe, "Comparative evaluation of three diphosphonates: *in vitro* adsorption (C-14 labeled) and *in vivo* osteogenic uptake (Tc-99m complexed)," *Journal of Nuclear Medicine*, vol. 21, no. 12, pp. 1185–1189, 1980.

[18] J. P. Lavender, R. A. A. Khan, and S. P. F. Hughes, "Blood flow and tracer uptake in normal and abnormal canine bone: comparisons with Sr-85 microspheres, Kr-81m, and Tc-99m MDP," *Journal of Nuclear Medicine*, vol. 20, no. 5, pp. 413–418, 1979.

[19] R. S. Budd, G. S. Hodgson, and W. S. C. Hare, "The relation of radionuclide uptake by bone to the rate of calcium mineralization. I: experimental studies using ^{45}Ca, ^{32}P and ^{99}Tc^{m}-MDP," *British Journal of Radiology*, vol. 62, no. 736, pp. 314–317, 1989.

[20] R. S. Budd, G. S. Hodgson, and W. S. C. Hare, "The relation of radionuclide uptake by bone to the rate of calcium mineralization. II: patient studies using ^{99}Tcm-MDP," *British Journal of Radiology*, vol. 62, no. 736, pp. 318–320, 1989.

[21] D. Kanishi, "^{99m}Tc-MDP accumulation mechanisms in bone," *Oral Surgery Oral Medicine and Oral Pathology*, vol. 75, no. 2, pp. 239–246, 1993.

[22] C. S. B. Galasko, "Mechanism of uptake of bone imaging isotopes by skeletal metastases," *Clinical Nuclear Medicine*, vol. 5, no. 12, pp. 565–568, 1980.

[23] S. Tanabe, J. P. Zodda, and E. Deutsch, "Effect of pH on the formation of Tc(NaBH4)-MDP radiopharmaceutical analogues," *International Journal of Applied Radiation and Isotopes*, vol. 34, no. 12, pp. 1577–1584, 1983.

[24] G. M. Wilson and T. C. Pinkerton, "Determination of charge and size of technetium diphosphonate complexes by anion-exchange liquid chromatography," *Analytical Chemistry*, vol. 57, no. 1, pp. 246–253, 1985.

[25] T. C. Pinkerton, K. T. Cheng, S. M. Shaw, and G. M. Wilson, "Influence of complex charge and size on the uptake of ^{99m}Tc-diphosphonates in osteogenic tissue," *International Journal of Radiation Applications and Instrumentation*, vol. 13, no. 1, pp. 49–56, 1986.

[26] J. L. Meyer and G. H. Nancollas, "The influence of multidentate organic phosphonates on the crystal growth of hydroxyapatite," *Calcified Tissue International*, vol. 13, no. 4, pp. 295–303, 1973.

[27] K. Libson, E. Deutsch, and B. L. Barnett, "Structural characterization of a 99Tc-diphosphonate complex. Implications for the chemistry of 99mTc skeletal imaging agents," *Journal of the American Chemical Society*, vol. 102, no. 7, pp. 2476–2478, 1980.

[28] K. Verbeke, J. Rozenski, B. Cleynhens et al., "Development of a conjugate of ^{99m}Tc-EC with aminomethylenediphosphonate in the search for a bone tracer with fast clearance from soft tissue," *Bioconjugate Chemistry*, vol. 13, no. 1, pp. 16–22, 2002.

[29] K. Ogawa, T. Mukai, Y. Inoue, M. Ono, and H. Saji, "Development of a novel ^{99m}Tc-chelate-conjugated bisphosphonate with high affinity for bone as a bone scintigraphic agent," *Journal of Nuclear Medicine*, vol. 47, no. 12, pp. 2042–2047, 2006.

[30] E. Palma, B. L. Oliveira, J. D. G. Correia et al., "A new bisphosphonate-containing ^{99m}Tc(I) tricarbonyl complex potentially useful as bone-seeking agent: synthesis and biological evaluation," *Journal of Biological Inorganic Chemistry*, vol. 12, no. 5, pp. 667–679, 2007.

[31] R. Torres Martin De Rosales, C. Finucane, S. J. Mather, and P. J. Blower, "Bifunctional bisphosphonate complexes for the diagnosis and therapy of bone metastases," *Chemical Communications*, no. 32, pp. 4847–4849, 2009.

[32] K. P. Zhernosekov, D. V. Filosofov, R. P. Baum et al., "Processing of generator-produced ^{68}Ga for medical application," *Journal of Nuclear Medicine*, vol. 48, no. 10, pp. 1741–1748, 2007.

[33] R. T. Goulet, A. Shysh, A. A. Noujaim, and B. C. Lentle, "Investigation of ^{68}Ga tripolyphosphate as a potential bone scanning agent," *International Journal of Applied Radiation and Isotopes*, vol. 26, no. 4, pp. 195–199, 1975.

[34] M. K. Dewanjee, D. J. Hnatowich, and R. Beh, "New ^{68}Ga labeled skeletal imaging agents for positron scintigraphy," *Journal of Nuclear Medicine*, vol. 17, no. 11, pp. 1003–1007, 1976.

[35] M. Mitterhauser, S. Toegel, W. Wadsak et al., "Pre vivo, ex vivo and *in vivo* evaluations of [^{68}Ga]-EDTMP," *Nuclear Medicine and Biology*, vol. 34, no. 4, pp. 391–397, 2007.

[36] M. Fellner, R. P. Baum, V. Kubíček et al., "PET/CT imaging of osteoblastic bone metastases with 68Ga- bisphosphonates: first human study," *European Journal of Nuclear Medicine and Molecular Imaging*, vol. 37, no. 4, p. 834, 2010.

[37] K. Ogawa, K. Takai, H. Kanbara et al., "Preparation and evaluation of a radiogallium complex-conjugated bisphosphonate as a bone scintigraphy agent," *Nuclear Medicine and Biology*, vol. 38, no. 5, pp. 631–636, 2011.

[38] M. Blau, W. Nagler, and M. A. Bender, "Fluorine-18: a new isotope for bone scanning," *Journal of Nuclear Medicine*, vol. 3, pp. 332–334, 1962.

[39] A. G. Jones, M. D. Francis, and M. A. Davis, "Bone scanning: radionuclidic reaction mechanisms," *Seminars in Nuclear Medicine*, vol. 6, no. 1, pp. 3–18, 1976.

[40] S. Bang and C. A. Baud, "Topographical distribution of fluoride in iliac bone of a fluoride-treated osteoporotic patient," *Journal of Bone and Mineral Research*, vol. 5, no. 1, pp. S87–S89, 1990.

[41] G. M. Blake, S. J. Park-Holohan, G. J. R. Cook, and I. Fogelman, "Quantitative studies of bone with the use of ^{18}F-fluoride and ^{99m}Tc-methylene diphosphonate," *Seminars in Nuclear Medicine*, vol. 31, no. 1, pp. 28–49, 2001.

[42] H. Schirrmeister, A. Guhlmann, K. Elsner et al., "Sensitivity in detecting osseous lesions depends on anatomic localization:

planar bone scintigraphy versus ^{18}F PET," *Journal of Nuclear Medicine*, vol. 40, no. 10, pp. 1623–1629, 1999.

[43] H. Schirrmeister, A. Guhlmann, J. Kotzerke et al., "Early detection and accurate description of extent of metastatic bone disease in breast cancer with fluoride ion and positron emission tomography," *Journal of Clinical Oncology*, vol. 17, no. 8, pp. 2381–2389, 1999.

Bioorganic & Medicinal Chemistry Letters 21 (2011) 6519–6522

Contents lists available at SciVerse ScienceDirect

Bioorganic & Medicinal Chemistry Letters

journal homepage: www.elsevier.com/locate/bmcl

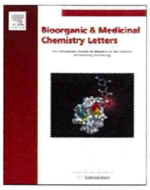

A dual fluorinated and iodinated radiotracer for PET and SPECT imaging of β-amyloid plaques in the brain

Hiroyuki Watanabe [a,b], Masahiro Ono [a,b,*], Hiroyuki Kimura [a], Shinya Kagawa [c], Ryuichi Nishii [c], Takeshi Fuchigami [b], Mamoru Haratake [b], Morio Nakayama [b,*], Hideo Saji [a]

[a] *Department of Patho-Functional Bioanalysis, Graduate School of Pharmaceutical Sciences, Kyoto University, 46-29 Yoshida Shimoadachi-cho, Sakyo-ku, Kyoto 606-8501, Japan*
[b] *Department of Hygienic Chemistry, Graduate School of Biomedical Sciences, Nagasaki University, 1-14 Bunkyo-machi, Nagasaki 852-8521, Japan*
[c] *Shiga Medical Center Research Institute, 5-4-30 Moriyama, Moriyama City, Shiga 524-8524, Japan*

ARTICLE INFO

Article history:
Received 31 May 2011
Revised 12 August 2011
Accepted 13 August 2011
Available online 24 August 2011

Keywords:
Alzheimer's disease
β-Amyloid peptide
PET
SPECT
Dual imaging

ABSTRACT

We report a fluorinated and iodinated radiotracer as a probe for PET/SPECT to detect of β-amyloid (Aβ) plaques in the brain of patients with Alzheimer's disease (AD). We successfully designed and synthesized the fluorinated and iodinated aurone derivative (**3**) and its radiolabels ($[^{125}\text{I}]$**3** and $[^{18}\text{F}]$**3**). In binding experiments in vitro, **3** showed high affinity for Aβ aggregates (K_i = 6.81 nM). In brain sections of AD model mice, **3** intensely stained Aβ plaques. Furthermore, a specific plaque labeling signal was observed on the autoradiography of postmortem AD brain sections using $[^{125}\text{I}]$**3**. In biodistribution experiments using normal mice, $[^{125}\text{I}]$**3** and $[^{18}\text{F}]$**3** displayed good uptake into and a rapid washout from the brain, properties highly desirable for Aβ imaging agents. These results suggest that **3** may function as a PET/SPECT dual imaging agent for detecting Aβ plaques in AD brains.

Alzheimer's disease (AD) is a progressive neurodegenerative disorder characterized by cognitive decline, irreversible memory loss, disorientation, and language impairment. Senile plaques containing β-amyloid (Aβ) peptides and neurofibrillary tangles in postmortem brain are two pathological hallmarks of AD.[1,2] Excessive production of Aβ via various normal or abnormal mechanisms is considered to be the initial neurodegenerative event in AD. Currently, it is difficult for clinicians to differentiate between the cognitive decline associated with normal aging and the cognitive decline associated with AD. There is no simple and definitive diagnostic method to detect Aβ plaques in the brain without postmortem pathological staining of brain tissue. Thus, the development of imaging agents for positron emission tomography (PET) or single photon emission computed tomography (SPECT), which can detect Aβ plaques in vivo may assist with the early diagnosis of AD.[3–5]

The nuclear imaging modality of choice in the clinic is often PET rather than SPECT in part because of superior sensitivity, resolution, and quantitative ability. Therefore, in the past few years, several groups' efforts have focused on the development of potential PET probes for the detection of Aβ plaques in vivo. As a result, PET probes such as $[^{18}\text{F}]$AV-45,[6,7] $[^{18}\text{F}]$GE-068,[8] $[^{18}\text{F}]$BAY94-9172,[9,10] $[^{11}\text{C}]$AZD2184,[11,12] $[^{11}\text{C}]$PIB,[13,14] $[^{11}\text{C}]$SB-13,[15,16] and $[^{18}\text{F}]$FDDNP[17,18] have been tested clinically and demonstrated potential utility for the diagnosis of AD. Conversely, more SPECT scanners have been installed for routine clinical imaging than PET imaging devices, which provides a certain advantage to the use of SPECT imaging agents. Therefore, SPECT is thought to be more valuable than PET in terms of routine diagnostic use. While the development of more useful Aβ imaging probes for SPECT has been a critical issue, $[^{123}\text{I}]$IMPY is the only SPECT probe to be tested in humans.[19–21] The preliminary clinical data for $[^{123}\text{I}]$IMPY showed a poor signal-to-noise ratio making it difficult to distinguish AD patients, possibly due to high lipophilicity and low stability.

Although many PET or SPECT imaging probes for cerebral Aβ plaques have been reported, there has been no report on the development of dual imaging probes. To develop novel radiotracers offering both PET (^{18}F) and SPECT (^{123}I) imaging using a single compound, we designed a new candidate compound which has both fluoride and iodide in a single chemical structure. We have recently reported the use of radioiodinated aurone derivatives as a new backbone structure in the development of Aβ imaging probes for SPECT.[22,23] The derivatives showed strong binding to Aβ aggregates, good penetration of the brain, and a fast washout from the brain despite their substituted groups. Among them, AR-1 (Fig. 1) showed the most promising characteristics as a SPECT probe in terms of affinity for Aβ aggregates and radioactivity pharmacokinetics in the brain.

---

* Corresponding authors. Tel.: +81 75 753 4608; fax: +81 75 753 4568 (M.O.); tel./fax: +81 95 819 2441 (M.N.).
E-mail addresses: ono@pharm.kyoto-u.ac.jp (M. Ono), morio@nagasaki-u.ac.jp (M. Nakayama).

0960-894X/$ - see front matter © 2011 Elsevier Ltd. All rights reserved.
doi:10.1016/j.bmcl.2011.08.063

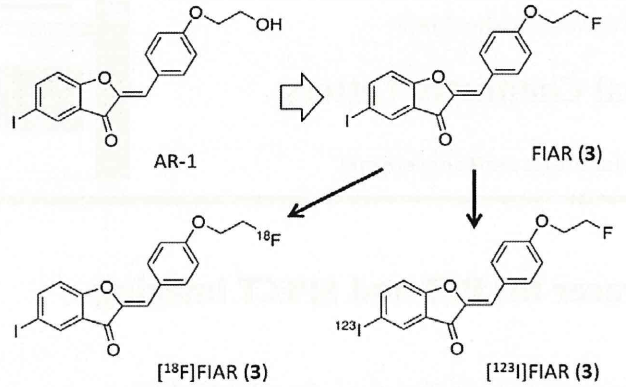

Figure 1. Flow chart of the development of PET/SPECT dual imaging probes for Aβ plaques.

In the present study, we designed and synthesized a new fluorinated and iodinated aurone derivative (FIAR) with a 2-fluoroethoxy group at the 4′ position of AR-1 (Fig. 1) and evaluated its biological potential as a PET/SPECT dual imaging probe for Aβ by testing its affinity for Aβ aggregates in vitro and its uptake by and clearance from the brain in biodistribution experiments using normal mice.

The target aurone derivatives were prepared as shown in Schemes 1 and 2. The synthesis of the aurone backbone was achieved by an Aldol reaction of benzofuranone with benzaldehyde using Al_2O_3.[24] In this process, 5-iodobenzofuran-3(2*H*)-one was reacted with 4-(2-fluoroethoxy)benzaldehyde **2** or 4-(2-hydroxyethoxy)benzaldehyde **1** in the presence of Al_2O_3 in chloroform at room temperature to form **3** and **5** in yields of 27% and 48%, respectively. The tributyltin derivative **4** was prepared from the corresponding compound **3** using a halogen to tributyltin exchange reaction catalyzed by Pd(0) for yields of 32.2%. The tributyltin derivative was used as the starting material for radioiodination in the preparation of [^{125}I]**3**. [^{125}I]**3** was achieved by an iododestannylation reaction using hydrogen peroxide as the oxidant, which produced the desired radioiodinated ligand (Scheme 1). It was anticipated that the no-carrier-added preparation would result in a final product bearing a theoretical specific activity similar to that of ^{125}I (2200 Ci/mmol). The free OH groups of **5** were converted into tosylates by reacting with TsCl in the presence of pyridine to give **6**. To make the desired ^{18}F-labeled aurone, [^{18}F]**3**, the tosylate **6** was employed as the precursor. A solution of **6** in acetonitrile (200 μL) was added to a reaction vessel containing ^{18}F and the mixture was heated at 100 °C for 10 min (Scheme 2). The radiochemical identity of [^{125}I]**3** and [^{18}F]**3** was verified by a comparison of retention times with the nonradioactive compound. These products were obtained in >23% radiochemical yields with a radiochemical purity of >95% after purification by HPLC.

In vitro binding experiments to evaluate the affinity of the aurone derivative **3** for Aβ aggregates were carried out in solution with [^{125}I]IMPY as the ligand. The compound inhibited the binding of [^{125}I]IMPY to Aβ(1–42) aggregates in a dose-dependent manner, indicating an affinity for Aβ aggregates (Fig. 2). The K_i value estimated for **3** was 6.81 nM. This value suggested that **3** had binding affinity sufficient for the in vivo imaging of Aβ(1–42) aggregates in the brain. The affinity was in the same range as that of aurone derivatives reported previously,[22,23] indicating no decrease in binding even though the iodide and the fluoroethoxy group were both introduced into the aurone scaffold.

To confirm the affinity of aurone derivatives for Aβ plaques in the mouse brain, neuropathological staining with **3** was carried out using brain sections from transgenic mouse (*Tg2576*) (Fig. 3). Many Aβ plaques were clearly stained with **3**, as reflected by the high affinity for Aβ aggregates in inhibition assays in vitro (Fig. 3A). The labeling pattern of **3** was consistent with that of thioflavin-S, a dye commonly used for the detection of Aβ plaques (Fig. 3B), indicating that **3** has affinity for Aβ plaques in the mouse brain in addition to having binding affinity for synthetic Aβ42 aggregates. Conversely, no apparent staining of **3** was observed in age-matched control mouse brain sections (Fig. 3C).

Furthermore, we investigated the affinity of [^{125}I]**3** for Aβ plaques by in vitro autoradiography in human AD brain sections (Fig. 4). The autoradiographic images of [^{125}I]**3** showed high levels

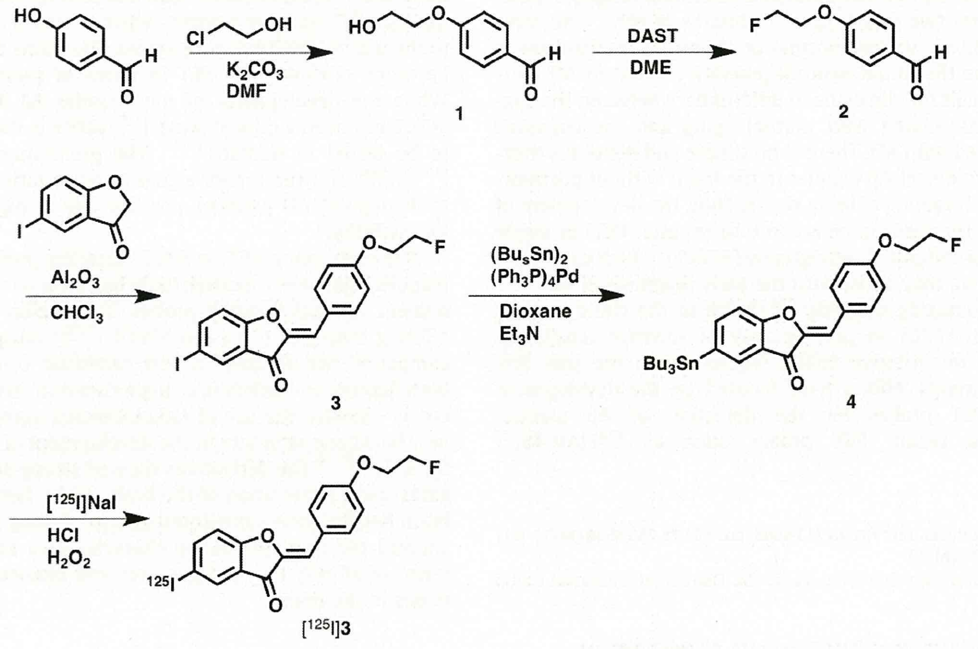

Scheme 1. Synthesis of [^{125}I]**3**.

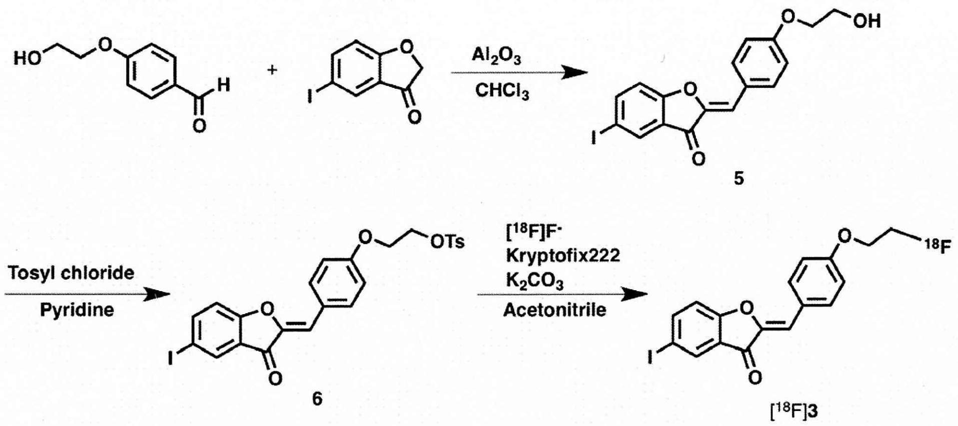

Scheme 2. Synthesis of $[^{18}F]$**3**.

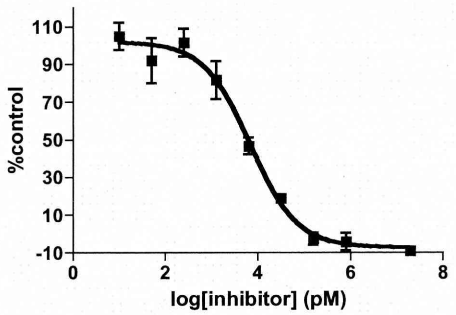

Figure 2. Competition curve for **3** against $[^{125}I]$IMPY.

of radioactivity in the brain sections (Fig. 4A). We confirmed that the hot spots of $[^{125}I]$**3** corresponded with those of in vitro immunohistochemical staining (Fig. 4B). In contrast, normal human brain displayed no remarkable accumulation of $[^{125}I]$**3** (Fig. 4C). These results demonstrate the feasibility of using **3** as a probe for detecting Aβ plaques in the brains of AD patients by PET/SPECT.

The biodistribution of $[^{125}I]$**3** and $[^{18}F]$**3** in vivo was tested in normal mice (Table 1). A biodistribution study provides important information on brain uptake. The ideal Aβ imaging probe should have good blood–brain barrier penetration to deliver a sufficient dose into the brain while achieving rapid clearance from normal regions to result in a higher signal-to-noise ratio in the AD brain. The initial brain uptake of $[^{125}I]$**3** was 2.34% of injected dose/gram at 2 min postinjection, whereas the radioactivity accumulated in the brain was rapidly eliminated (0.19% of injected dose/gram at 60 min postinjection), properties highly desirable for Aβ imaging probes. $[^{18}F]$**3** displayed high uptake (3.66% of injected dose/gram at 2 min postinjection) into and rapid clearance (1.75% of injected

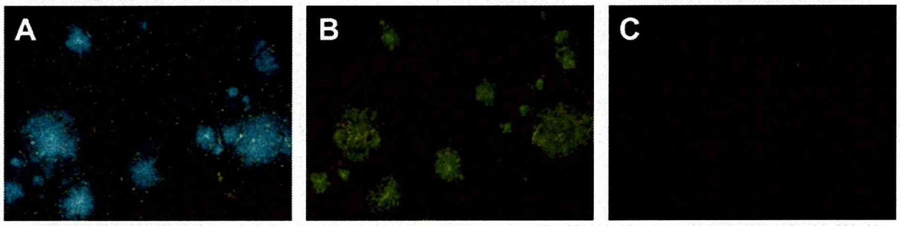

Figure 3. Fluorescent staining of **3** in 10-μm *Tg2576* mouse brain sections (A). Labeled plaques were confirmed by staining of the adjacent sections with thioflavin-S (B). No apparent staining of **3** was observed in the age-matched control mouse brain section (C).

Figure 4. In vitro ARG of $[^{125}I]$**3** revealed the distinct labeling of Aβ plaques in AD brain sections (A). The presence and localization of plaques in the sections were confirmed with immunohistochemical staining using a monoclonal β-amyloid antibody (B). Conversely, there was very little labeling of $[^{125}I]$**3** in a control brain section (C).

Table 1
Biodistribution of radioactivity after injection of [^{125}I]**3** and [^{18}F]**3** in normal mice[a]

Tissue	Time after injection (min)			
	2	10	30	60
[^{125}I]**3** (log $P = 2.45 \pm 0.04$)[b]				
Blood	6.70 (2.97)	3.13 (0.58)	1.94 (0.21)	1.29 (0.14)
Liver	17.06 (1.48)	16.50 (1.65)	12.44 (0.72)	10.96 (2.06)
Kidney	6.96 (0.76)	7.53 (0.85)	5.49 (1.21)	5.22 (1.95)
Intestine	2.02 (0.48)	6.53 (1.44)	12.35 (1.21)	15.74 (1.12)
Spleen	3.74 (0.48)	4.33 (0.87)	3.61 (0.85)	2.37 (0.59)
Pancreas	3.44 (0.58)	1.33 (0.33)	0.80 (0.16)	1.35 (0.09)
Heart	4.90 (0.86)	1.95 (0.26)	1.54 (0.22)	1.19 (0.53)
Stomach[c]	0.61 (0.07)	1.46 (1.85)	0.79 (0.51)	0.89 (0.35)
Brain	2.34 (0.36)	0.84 (0.23)	0.19 (0.03)	0.12 (0.06)
[^{18}F]**3**				
Blood	5.72 (1.14)	2.84 (0.19)	2.68 (0.39)	2.61 (0.27)
Brain	3.66 (0.19)	2.37 (0.12)	1.77 (0.39)	1.75 (0.22)
Bone	2.03 (0.20)	2.13 (0.16)	3.45 (1.50)	3.42 (0.42)

[a] Expressed as % injected dose per gram. Each value represents the mean (SD) for 5–6 animals.

[b] Octanol/buffer (0.1 M phosphate-buffered saline, pH 7.4) partition coefficients. Each value represents the mean (SD) for three experiments.

[c] Expressed as % injected dose per organ.

dose/gram at 60 min postinjection) from brain. [^{125}I]**3** and [^{18}F]**3** showed different radioactivity pharmacokinetics in the brain despite of their similar chemical structure. This could be attributable to the difference in the physicochemical characteristics of their radiometabolites produced after injection of [^{125}I]**3** and [^{18}F]**3** in vivo, but the precise reason remains unclear. However, data for **3** on radioactivity pharmacokinetics in the brain support the further development of dual probes for PET (^{18}F) and SPECT (^{123}I) based on various Aβ-binding scaffolds using a single chemical structure.

In conclusion, we successfully designed and synthesized a fluorinated and iodinated aurone derivative as a probe for PET and SPECT to detect Aβ plaques in the brain. In binding experiments in vitro, **3** showed high affinity for Aβ aggregates. The aurone derivatives clearly stained Aβ plaques in an animal model of AD, reflecting their affinity for Aβ aggregates in vitro. In biodistribution experiments using normal mice, [^{125}I]**3** displayed good uptake in and fast washout from the brain. [^{18}F]**3** also displayed high uptake in and good washout from brain, although a slight difference was observed between the ^{125}I and ^{18}F tracers. A specific plaque labeling signal was clearly depicted by [^{125}I]**3** in postmortem AD brain sections. Taken together, the present results suggested that the fluorinated and iodinated aurone derivative may function as a PET/SPECT probe for detecting Aβ plaques in the AD brain.

Acknowledgments

The study was supported by the Funding Program for Next Generation World-Leading Researchers (NEXT Program), and a Grant-in-aid for Young Scientists (A) and Exploratory Research from the Ministry of Education, Culture, Sports, Science and Technology, Japan.

Supplementary data

Supplementary data (procedure for the preparation of FIAR, in vitro binding assay, in vitro autoradiography using AD brain sections, and biodistribution studies) associated with this article can be found, in the online version, at doi:10.1016/j.bmcl.2011.08.063.

References and notes

1. Klunk, W. E. *Neurobiol. Aging* **1998**, *19*, 145.
2. Selkoe, D. J. *Physiol. Rev.* **2001**, *81*, 741.
3. Selkoe, D. J. *Nat. Biotechnol.* **2000**, *18*, 823.
4. Mathis, C. A.; Wang, Y.; Klunk, W. E. *Curr. Pharm. Des.* **2004**, *10*, 1469.
5. Nordberg, A. *Lancet Neurol.* **2004**, *3*, 519.
6. Kung, H. F.; Choi, S. R.; Qu, W.; Zhang, W.; Skovronsky, D. *J. Med. Chem.* **2010**, *53*, 933.
7. Choi, S. R.; Golding, G.; Zhuang, Z.; Zhang, W.; Lim, N.; Hefti, F.; Benedum, T. E.; Kilbourn, M. R.; Skovronsky, D.; Kung, H. F. *J. Nucl. Med.* **2009**, *50*, 1887.
8. Koole, M.; Lewis, D. M.; Buckley, C.; Nelissen, N.; Vandenbulcke, M.; Brooks, D. J.; Vandenberghe, R.; Van Laere, K. *J. Nucl. Med.* **2009**, *50*, 818.
9. Zhang, W.; Oya, S.; Kung, M. P.; Hou, C.; Maier, D. L.; Kung, H. F. *Nucl. Med. Biol.* **2005**, *32*, 799.
10. Rowe, C. C.; Ackerman, U.; Browne, W.; Mulligan, R.; Pike, K. L.; O'Keefe, G.; Tochon-Danguy, H.; Chan, G.; Berlangieri, S. U.; Jones, G.; Dickinson-Rowe, K. L.; Kung, H. P.; Zhang, W.; Kung, M. P.; Skovronsky, D.; Dyrks, T.; Holl, G.; Krause, S.; Friebe, M.; Lehman, L.; Lindemann, S.; Dinkelborg, L. M.; Masters, C. L.; Villemagne, V. L. *Lancet Neurol.* **2008**, *7*, 129.
11. Johnson, A. E.; Jeppsson, F.; Sandell, J.; Wensbo, D.; Neelissen, J. A.; Jureus, A.; Strom, P.; Norman, H.; Farde, L.; Svensson, S. P. *J. Neurochem.* **2009**, *108*, 1177.
12. Nyberg, S.; Jonhagen, M. E.; Cselenyi, Z.; Halldin, C.; Julin, P.; Olsson, H.; Freund-Levi, Y.; Andersson, J.; Varnas, K.; Svensson, S.; Farde, L. *Eur. J. Nucl. Med. Mol. Imaging* **2009**, *36*, 1859.
13. Mathis, C. A.; Wang, Y.; Holt, D. P.; Huang, G. F.; Debnath, M. L.; Klunk, W. E. *J. Med. Chem.* **2003**, *46*, 2740.
14. Klunk, W. E.; Engler, H.; Nordberg, A.; Wang, Y.; Blomqvist, G.; Holt, D. P.; Bergstrom, M.; Savitcheva, I.; Huang, G. F.; Estrada, S.; Ausen, B.; Debnath, M. L.; Barletta, J.; Price, J. C.; Sandell, J.; Lopresti, B. J.; Wall, A.; Koivisto, P.; Antoni, G.; Mathis, C. A.; Langstrom, B. *Ann. Neurol.* **2004**, *55*, 306.
15. Ono, M.; Wilson, A.; Nobrega, J.; Westaway, D.; Verhoeff, P.; Zhuang, Z. P.; Kung, M. P.; Kung, H. F. *Nucl. Med. Biol.* **2003**, *30*, 565.
16. Verhoeff, N. P.; Wilson, A. A.; Takeshita, S.; Trop, L.; Hussey, D.; Singh, K.; Kung, H. F.; Kung, M. P.; Houle, S. *Am. J. Geriatr. Psychiatry* **2004**, *12*, 584.
17. Agdeppa, E. D.; Kepe, V.; Liu, J.; Flores-Torres, S.; Satyamurthy, N.; Petric, A.; Cole, G. M.; Small, G. W.; Huang, S. C.; Barrio, J. R. *J. Neurosci.* **2001**, *21*, RC189.
18. Shoghi-Jadid, K.; Small, G. W.; Agdeppa, E. D.; Kepe, V.; Ercoli, L. M.; Siddarth, P.; Read, S.; Satyamurthy, N.; Petric, A.; Huang, S. C.; Barrio, J. R. *Am. J. Geriatr. Psychiatry* **2002**, *10*, 24.
19. Kung, M. P.; Hou, C.; Zhuang, Z. P.; Zhang, B.; Skovronsky, D.; Trojanowski, J. Q.; Lee, V. M.; Kung, H. F. *Brain Res.* **2002**, *956*, 202.
20. Zhuang, Z. P.; Kung, M. P.; Wilson, A.; Lee, C. W.; Plossl, K.; Hou, C.; Holtzman, D. M.; Kung, H. F. *J. Med. Chem.* **2003**, *46*, 237.
21. Newberg, A. B.; Wintering, N. A.; Plossl, K.; Hochold, J.; Stabin, M. G.; Watson, M.; Skovronsky, D.; Clark, C. M.; Kung, M. P.; Kung, H. F. *J. Nucl. Med.* **2006**, *47*, 748.
22. Ono, M.; Maya, Y.; Haratake, M.; Ito, K.; Mori, H.; Nakayama, M. *Biochem. Biophys. Res. Commun.* **2007**, *361*, 116.
23. Maya, Y.; Ono, M.; Watanabe, H.; Haratake, M.; Saji, H.; Nakayama, M. *Bioconjugate Chem.* **2009**, *20*, 95.
24. Bryant, W. M.; Huhn, G. F. *Synth. Commun.* **1995**, *25*, 915.

Cancer Science
The official journal of the Japanese Cancer Association

Evaluation of [^{125}I]IPOS as a molecular imaging probe for hypoxia-inducible factor-1-active regions in a tumor: Comparison among single-photon emission computed tomography/X-ray computed tomography imaging, autoradiography, and immunohistochemistry

Masashi Ueda,[1,2] Takashi Kudo,[2] Yasuko Mutou,[3] Izumi Ogihara Umeda,[3] Azusa Miyano,[2] Kei Ogawa,[2] Masahiro Ono,[2] Hirofumi Fujii,[3] Shinae Kizaka-Kondoh,[4] Masahiro Hiraoka[5] and Hideo Saji[2,6]

[1]Radioisotopes Research Laboratory, Kyoto University Hospital, Faculty of Medicine, Kyoto University, Kyoto; [2]Department of Patho-Functional Bioanalysis, Graduate School of Pharmaceutical Sciences, Kyoto University, Kyoto; [3]Functional Imaging Division, Research Center for Innovative Oncology, National Cancer Center Hospital East, Kashiwa; [4]Department of Biomolecular Engineering, Graduate School of Bioscience and Biotechnology, Tokyo Institute of Technology, Yokohama; [5]Department of Radiation Oncology and Image-Applied Therapy, Graduate School of Medicine, Kyoto University, Kyoto, Japan

(Received March 10, 2011/Revised July 26, 2011/Accepted August 2, 2011/Accepted manuscript online August 8, 2011/Article first published online September 15, 2011)

To image hypoxia-inducible factor-1 (HIF-1)-active tumors, we previously developed a chimeric protein probe ([$^{123/125}$I]IPOS) that is degraded in the same manner as HIF-1α under normoxic conditions. In the present study, we aim to show that the accumulation of radioiodinated POS reflects the expression of HIF-1. *In vivo* single-photon emission computed tomography (SPECT)/X-ray CT (CT) imaging, autoradiography, and double-fluorescent immunostaining for HIF-1α and pimonidazole (PIMO) were carried out 24 h after the injection of [^{125}I]IPOS. Tumor metabolite analysis was also carried out. A tumor was clearly visualized by multi-pinhole, high-resolution SPECT/CT imaging with [^{125}I]IPOS. The obtained images were in accordance with the corresponding autoradiograms and with the results of *ex vivo* biodistribution. A metabolite analysis revealed that 77% of the radioactivity was eluted in the macromolecular fraction, suggesting that the radioactivity mainly existed as [^{125}I]IPOS in the tumors. Immunohistochemistry revealed that the HIF-1α-positive areas and PIMO-positive areas were not always identical, only some of the regions were positive for both markers. The areas showing [^{125}I]IPOS accumulation were positively and significantly correlated with the HIF-1α-positive areas ($R = 0.75$, $P < 0.0001$). The correlation coefficient between [^{125}I]IPOS-accumulated areas and HIF-1α-positive areas was significantly greater than that between the [^{125}I]IPOS-accumulated areas and the PIMO-positive areas ($P < 0.01$). These findings indicate that [^{125}I]IPOS accumulation reflects HIF-1 expression. Thus, [$^{123/125}$I]IPOS can serve as a useful probe for the molecular imaging of HIF-1-active tumors. (*Cancer Sci* 2011; 102: 2090–2096)

The expansion of a tumor mass implies the development of cancer cells that are distant from blood vessels. Cells outgrow their vascular supply, leading to the lowering of oxygen partial pressure below physiologic levels (i.e., hypoxia). Hypoxia-inducible factor-1 (HIF-1) is a key transcriptional regulator in response to hypoxia.(1) Overexpression of HIF-1 has been indicated in over 70% of human cancers (e.g. breast, prostate, brain, lung, head and neck cancers) and their metastases compared to that of adjacent normal tissue.(2) Clinical studies associate the hypoxic status of a tumor with bad prognosis and resistance to chemotherapy and radiotherapy.(3) Furthermore, several HIF-1 inhibitors have been developed to inhibit tumor growth and to overcome resistance to therapies.(4) Thus, non-invasive imaging of HIF-1-active regions in a tumor provides useful information for qualitative cancer diagnosis, cancer therapy, and improving the effectiveness of HIF-1 inhibitors.

The expression of HIF-1 in tumors has been shown to be affected by the microenvironment in each tumor, resulting in heterogeneous HIF-1 tumor activity and expression.(5) Moreover, HIF-1 has been reported to be expressed even in a small tumor spheroid (<1 mm in diameter).(6) Therefore, a high spatial resolution device was required for the accurate imaging of HIF-1-expressed regions. Several techniques to improve spatial resolution, such as depth-of-interaction scintillators, image reconstruction using time-of-flight information, and multi-pinhole collimators, have recently been developed(7–10) and incorporated into commercially available PET and single-photon emission computed tomography (SPECT) systems. These modalities enable the detailed visualization of intratumoral HIF-1 expression in both animal models and humans.

Hypoxia-inducible factor-1 is composed of two subunits, HIF-1α and HIF-1β. The former is rapidly degraded by the ubiquitin–proteasome pathway under normoxic conditions, but it is stabilized under hypoxic conditions and regulates HIF-1 transcriptional activity. The proteasomal degradation of HIF-1α occurs through protein hydroxylation on proline residues in the oxygen-dependent degradation domain (ODD) of HIF-1α.(11,12) Thus, it is expected that probes containing the ODD and that are degraded in manner similar to HIF-1α can evaluate HIF-1 activity *in vivo*.

Based on the above concept, we recently developed a protein in which the protein transduction domain (PTD)(13) and a monomeric streptavidin (SAV) are fused to the ODD. We also synthesized a radiolabeled biotin derivative, (3-[$^{123/125}$I]iodobenzoyl)norbiotinamide ([$^{123/125}$I]IBB) and conjugated the chimeric protein, PTD-ODD-SAV (POS), and [$^{123/125}$I]IBB to produce [$^{123/125}$I]IBB-POS ([$^{123/125}$I]IPOS). POS was degraded in an oxygen-dependent manner, and a clear tumor image was obtained by planar imaging at 24 h after the injection of [^{123}I]IPOS. The intratumoral distribution of [^{125}I]IPOS corresponded to the hypoxic

---

[6] To whom correspondence should be addressed.
E-mail: hsaji@pharm.kyoto-u.ac.jp

doi: 10.1111/j.1349-7006.2011.02057.x

areas. However, direct comparison between the area showing $[^{125}I]$IPOS accumulation and HIF-1α expression was not carried out in the previous study.(14) Moreover, the 3D distribution of HIF-1-active regions in tumors has not been extensively evaluated *in vivo*. We then compared $[^{125}I]$IPOS distribution to HIF-1 expression by autoradiographic and immunohistochemical studies in the present study. Moreover, we attempted to image the detailed intratumoral distribution of $[^{125}I]$IPOS, which potentially reflects the heterogeneous expression of HIF-1, using a multi-pinhole, high-resolution small animal SPECT. The purpose of the present study is to reveal whether $[^{123/125}I]$IPOS can be used to visualize HIF-1-active regions in a tumor.

Materials and Methods

Animal model. Animal studies were carried out in accordance with our institutional guidelines, and the experimental procedures were approved by the Kyoto University Animal Care Committee (Kyoto, Japan) and the Ethical Committee for Animal Experiments of the National Cancer Center (Kashiwa, Japan). Five-week-old female C3H/He mice were purchased from Japan SLC (Hamamatsu, Japan) and kept at a constant ambient temperature under a 12-h light/dark cycle with free access to food and water. FM3A mouse mammary carcinoma cells were cultured and s.c. implanted in the right thigh as described in previous reports.(14,15) Approximately 2 weeks after the implantation, the mice were subjected to a tracer study. The average diameter of the tumors was 10 mm.

Radiosynthesis of $[^{125}I]$IPOS. POS was overexpressed in *Escherichia coli* and purified, as described in a previous report.(14) Purified POS was dissolved in Tris–HCl buffer (pH 8.0).

Sodium $[^{125}I]$iodide was purchased from PerkinElmer Life and Analytical Sciences (Boston, MA, USA). As described in a previous report,(14) $[^{125}I]$IBB was synthesized with a radiochemical yield of 40–50%. $[^{125}I]$IPOS was synthesized by incubation of $[^{125}I]$IBB and POS for 1 h followed by purification using Sephadex G50 columns (GE Healthcare Bioscience, Uppsala, Sweden). Using $[^{125}I]$IBB as a starting material, $[^{125}I]$IPOS was obtained with a radiochemical yield of >85% and a radiochemical purity of >95%.

***In vivo* and *ex vivo* SPECT/CT imaging.** Two FM3A-bearing mice were used in this study. They were i.v. injected with $[^{125}I]$IPOS (30 μg, 23 MBq), and 24 h later, CT and SPECT images were acquired under 1.5% isoflurane anesthesia. A SPECT/CT combined scanner was used to acquire sectional images; the scanner had four detectors equipped with tungsten-based, multiplexing multi-pinhole collimators dedicated for small animal imaging (NanoSPECT/CT; Bioscan, Washington, DC, USA).

First, CT scans were carried out under the following conditions: tube voltage, 45 kV; tube current, 177 μA; and tube current-time product (the product of tube current and scan time), 32 mAs. The obtained CT data were reconstructed using a cone-beam filtered back-projection method with InVivoScope (Bioscan) postprocessing software.

The SPECT scans were then carried out. In the SPECT system, each collimator had nine pinholes, each with a diameter of 1.4 mm and a cylindric field of view of 32 mm in diameter × 16 mm in length. The axial field of view was extended using a step-and-shoot helical SPECT with a user-defined range of up to 230 mm, based on the region to be imaged. The energy peak for the camera was set to 28 keV, and the energy window was set to peak energy ± 30%, that is, 20–36 keV. *In vivo* SPECT acquisition was carried out in six steps over 90° (300 s per step), with four detectors covering 360°. The total acquisition time to scan a range of 71.9 mm was 90 min per mouse. The acquired SPECT data were reconstructed with HiSPECT postprocessing software (SciVis, Göettingen, Germany) by an ordered subsets–expectation maximization algorithm designed for multiplexing multi-pinhole reconstruction.

Both SPECT and CT images were automatically coregistered because both systems shared the same axis of rotation, allowing for the combination of scintigraphic and anatomic information in all tomographic scans in three different spatial axes.

After *in vivo* imaging, the mice were killed and the tumors were carefully excised. The *ex vivo* SPECT image of each tumor was acquired for 60 min with an acquisition time of 600 s per projection. The tumors were then frozen and cut into 6-μm-thick sections for H&E staining and into 20-μm-thick sections for autoradiography. The sections were prepared in the same direction of the SPECT slice. The section corresponding to the SPECT image was selected according to the slice thickness and used for autoradiography.

***Ex vivo* biodistribution, autoradiography, and immunohistochemistry.** FM3A-bearing mice ($n = 5$) were i.v. injected with $[^{125}I]$IPOS (30 μg, 3.2 MBq); 22 h later, they were i.p. injected with pimonidazole (PIMO; 60 mg/kg). After another 2 h, the mice were killed. Whole organ specimens were immediately removed, weighed, and their radioactivity was measured with an auto-well gamma counter (Wizard 1480; PerkinElmer, Waltham, MA, USA). The results were expressed in terms of the percent injected dose per gram of tissue (%ID/g). The tumors were removed and divided into two parts. The radioactivity of one part was counted, and the other part was immediately frozen. After freezing, 10-μm-thick sections of tumor were prepared with a cryomicrotome (CM1900; Leica Microsystems, Wetzlar, Germany). Two sections were prepared from each tumor, and autoradiograms of these sections were obtained, according to a previously described method,(16,17) but with the following minor modification: a BAS5000 scanner was used instead of a BAS3000 scanner (both scanners; Fuji Photo Film, Tokyo, Japan). The same slides used in the autoradiographic study were subjected to dual fluorescent immunostaining for HIF-1α and PIMO.(15,18) Adjacent sections on each autoradiogram were stained with H&E to identify the necrotic regions.

Size-exclusion analysis of radioactive compounds in tumors. After an i.v. injection of $[^{125}I]$IPOS (30 μg, 4.4 MBq), FM3A-bearing mice ($n = 3$) were housed in metabolic cages (Metabolica; Sugiyama-Gen, Tokyo, Japan) for 24 h for the collection of urine and feces. Subsequently, the mice were killed. Extracts from the tumors and the feces were prepared by using a previously reported method,(15,18,19) with slight modifications. In brief, the tumors and feces were homogenized, and the preparations were centrifuged at 5000*g* at 4°C for 30 min. The supernatants and urine were analyzed by size-exclusion chromatography (PD-10; GE Healthcare Bioscience). In addition, aliquots of the supernatants from the tumors were analyzed by size-exclusion high-performance liquid chromatography (HPLC; TSKgel SuperSW2000; 4.6 × 300 mm; Tosoh, Tokyo, Japan) (100 mM phosphate buffer [pH 6.8], 0.2 mL/min).

Image analyses of autoradiograms and immunohistochemical images. Ten square regions of interest (ROIs) were selected from the viable regions that showed $[^{125}I]$IPOS accumulation on each autoradiogram and were then transferred to the corresponding immunohistochemical image. The positions of the ROIs in both images were confirmed on the basis of the x- and y-positions of each ROI that were displayed in both the softwares. The quantification of radioactivity in each ROI and the determination of the levels of HIF-1α expression and PIMO-adduct formation were carried out according to the previously reported method.(15)

Statistical analyses. Correlation coefficients were assessed using Spearman's rank analysis. A chi-square-test was used to compare the correlation coefficients between $[^{125}I]$IPOS-accumulated areas and HIF-1α- or PIMO-positive areas. Values of $P < 0.05$ were considered statistically significant.

Results

***In vivo* and *ex vivo* SPECT/CT imaging.** Representative SPECT/CT images are shown in Figure 1. The images indicate a clear and specific accumulation of radioactivity in the FM3A tumor at 24 h after [^{125}I]IPOS injection. Compared to the tumor, there was no [^{125}I]IPOS accumulation in the opposite leg (Fig. 1A,B,D). The serial axial images documented that the intratumoral distribution pattern of [^{125}I]IPOS was heterogeneous (Fig. 1E). The bladder can be seen in rostral-side slices.

Figure 2 shows *ex vivo* SPECT images and corresponding autoradiograms. Although autoradiograms showed intratumoral distribution of [^{125}I]IPOS in more detail due to its higher spatial resolution than SPECT images, a similar distribution pattern of [^{125}I]IPOS was observed in both images. Staining with H&E depicted necrotic regions in the tumor (Fig. 2, N), without the accumulation of [^{125}I]IPOS.

***Ex vivo* biodistribution.** Table 1 shows the biodistribution of [^{125}I]IPOS in FM3A xenografts at 24 h after injection. A high level of radioactivity was found to be accumulated in the liver and intestine, and a moderate level was present in the kidneys and tumor, and a low level was present in the muscle and neck. The tumor accumulation was 1.7%ID/g, the tumor/blood ratio was 5.6, and the tumor/muscle ratio was 10. These results were consistent with those of a previous report.(14)

Size-exclusion analysis of radioactive compounds in tumors. The recovery of radioactivity from tumor homogenates was 83% (SD, 3.8%). In the analysis using PD-10, most of the radioactive material was eluted in macromolecular fractions (77% [10%]). Moreover, by size-exclusion HPLC analysis, radioactivity was detected at approximately 34 kDa, which is

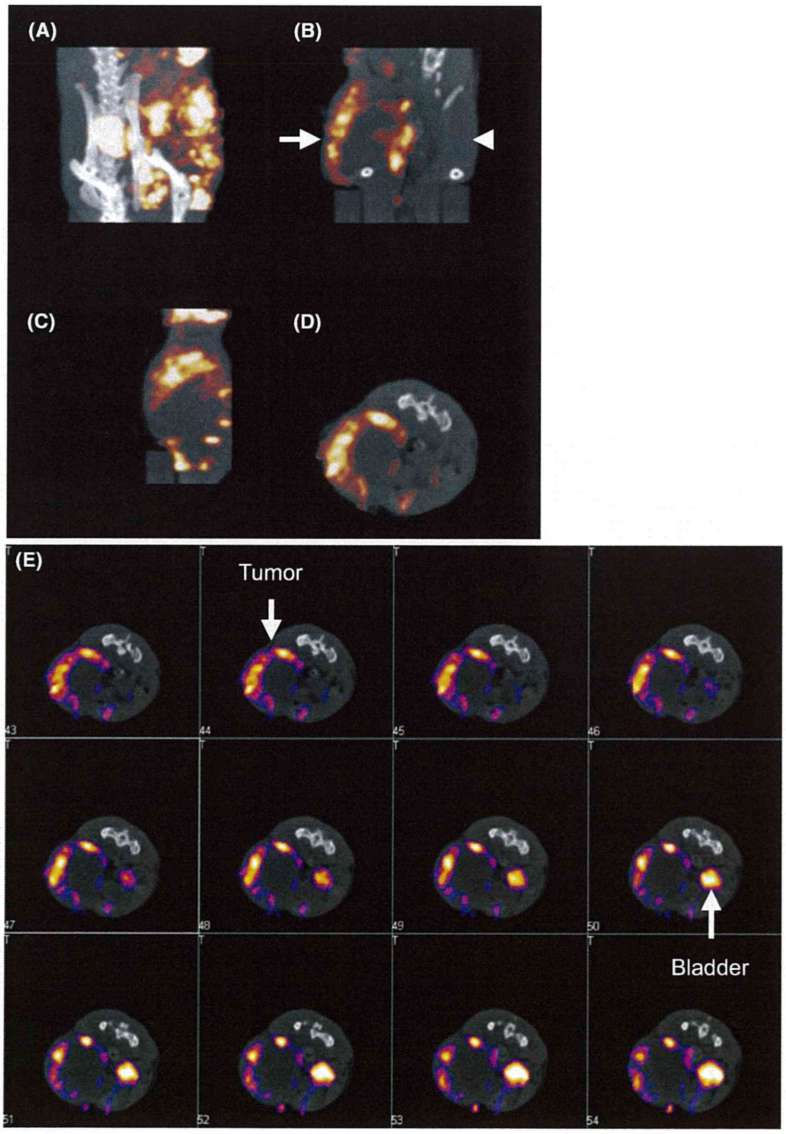

Fig. 1. Representative single-photon emission computed tomography/computed tomography fusion images of FM3A-bearing mouse obtained 24 h after injection of [^{125}I]IPOS. Maximum intensity projection (A), coronal (B), sagittal (C), and axial (D) images are shown. The arrow indicates the tumor in the right thigh, and the arrowhead indicates the corresponding area in the opposite leg in (B). Serial axial images (slice thickness, 0.3 mm) are also shown in (E).

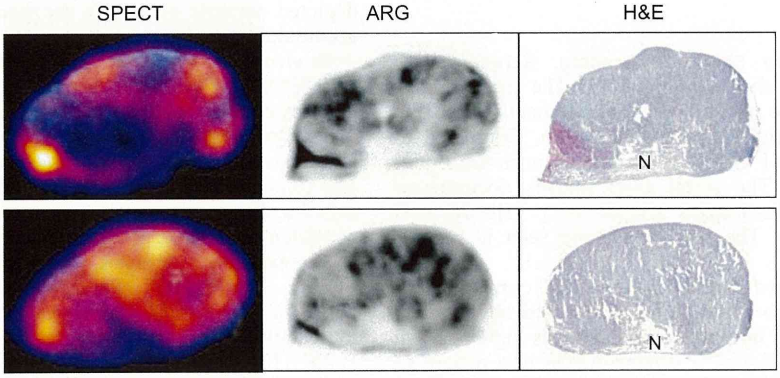

Fig. 2. *Ex vivo* single-photon emission computed tomography (SPECT) images with corresponding autoradiograms (ARG) and H&E stained sections. The images were obtained 25.5 h after injection of [^{125}I]IPOS. N, necrotic region.

Table 1. Biodistribution of [^{125}I]IPOS at 24 h in FM3A-xenografted mice (%ID/g)

Tissue	Radioactivity
Blood	0.31 ± 0.03
Liver	15.93 ± 1.11
Intestine	6.34 ± 1.55
Kidneys	3.40 ± 1.54
Tumor	1.71 ± 0.26
Muscle	0.18 ± 0.04
Neck†	0.10 ± 0.02
Urine†‡	45.85 ± 7.30
Feces†‡	26.27 ± 10.71
Tumor/blood ratio	5.57 ± 1.01
Tumor/muscle ratio	10.09 ± 2.82

Values are mean ± SD; n = 5. †Expressed as %ID. ‡n = 3.

the molecular weight of POS. In contrast, the radioactive material in feces homogenates and urine was rarely eluted in macromolecular fractions (5.6% [3.0%] and 0.36% [0.06%], respectively).

Autoradiography and immunohistochemistry. The autoradiogram represented that the distribution of [^{125}I]IPOS in the tumor was heterogeneous (Fig. 3A). Dual fluorescent immunohistochemistry indicated the presence of HIF-1α- and PIMO-positive hypoxic areas in the tumors (Fig. 3B,C). High-magnification merged imaging of HIF-1α and PIMO immunostaining revealed the presence of PIMO-positive areas along the edge of the HIF-1α-positive areas. However, HIF-1α-positive areas and PIMO-positive areas were not always identical. Some regions were positive for both, whereas other regions did not overlap (Fig. 3D). The majority of [^{125}I]IPOS-accumulated areas corresponded to the HIF-1α-positive areas (Fig. 3A,B).

We then compared correlations between [^{125}I]IPOS accumulation and HIF-1α or PIMO expression levels. As shown in Figure 4, areas with [^{125}I]IPOS accumulation showed a positive correlation with both HIF-1α- and PIMO-positive areas (HIF-1α: $R = 0.75$, $P < 0.0001$; PIMO: $R = 0.48$, $P = 0.0002$). The correlation coefficient between [^{125}I]IPOS and HIF-1α was significantly greater than that with PIMO ($\chi^2 = 8.38$, $P < 0.01$).

Discussion

A number of hypoxia imaging probes, such as [^{18}F]fluoromisonidazole ([^{18}F]FMISO), 1-α-D-(5-deoxy-5-[^{18}F]fluoroarabinofuranosyl)-2-nitroimidazole ([^{18}F]FAZA), and [$^{60/64}$Cu]Cu-diacetyl-bis(N^4-methylthiosemicarbazone) ([$^{60/64}$Cu]Cu-ATSM), have been developed and used in clinical studies.(20,21) These probes detect physically low oxygen partial pressure (<10 mmHg) and are useful for predicting the efficacy of radiotherapy.(22) In fact, clinical PET studies with [^{60}Cu]Cu-ATSM have shown an inverse relationship between the tumor uptake of [^{60}Cu]Cu-ATSM and the response to therapy in patients with lung and rectal carcinomas.(21) However, the mechanisms underlying hypoxic accumulation of these probes are not dependent on HIF-1 expression and further studies are necessary to decisively determine the role of them in identifying HIF-1-active regions in tumors.

The expression level of HIF-1α was reported to increase dramatically as the oxygen partial pressure decreased below 40 mmHg.(23) Furthermore, it was reported that the oxygen concentrations at which HIF-1 activity occurs differ among tissue cells.(3,23) For example, pulmonary cells are consistently exposed to relatively high oxygen concentrations, and thus, the oxygen concentrations that these cells perceive as abnormal are relatively high. However, bone marrow cells, which usually exist under low oxygen concentrations, require no HIF-1 activity when they are kept under the same oxygen concentrations as pulmonary cells.(5) Therefore, probes that detect absolute physical oxygen partial pressures are not enough when attempting to detect the expression or activity of HIF-1. Because HIF-1 is associated with tumor progression, angiogenesis, metastasis, and resistance to chemo- and radiotherapy, HIF-1 imaging would provide significant information for characterizing tumor phenotype and would be useful for predicting prognosis. Thus, multiple details on tumor characterization, treatment strategy, and prognosis would be provided by linking [^{123}I]IPOS-SPECT with [^{18}F]FMISO-, [^{18}F]FAZA-, or [$^{60/64}$Cu]Cu-ATSM-PET.

Recently, nuclear medical imaging(24–26) and bioluminescent imaging(27,28) based on HIF-1-responsive reporter systems have been successfully carried out. However, these systems required exogenous gene transfection. To surmount this limitation, our research group developed a number of injectable protein probes, including [^{125}I]IPOS, which contain ODD and degrade in an oxygen-dependent manner. These probes have been used successfully to visualize hypoxic tumors on planar nuclear medical imaging(14,15) and optical imaging.(1,5,29) However, the *in vivo* 3D distribution of HIF-1-active regions in tumors has not been extensively evaluated in our previous studies. Thus, we were challenged to obtain high spatial resolution tomographic images using multi-pinhole SPECT. Multi-pinhole SPECT systems have recently provided greatly improved efficiency with high spatial resolution and have overcome the resolution versus sensitivity trade-off.(30) The disadvantage of SPECT is a quantitative

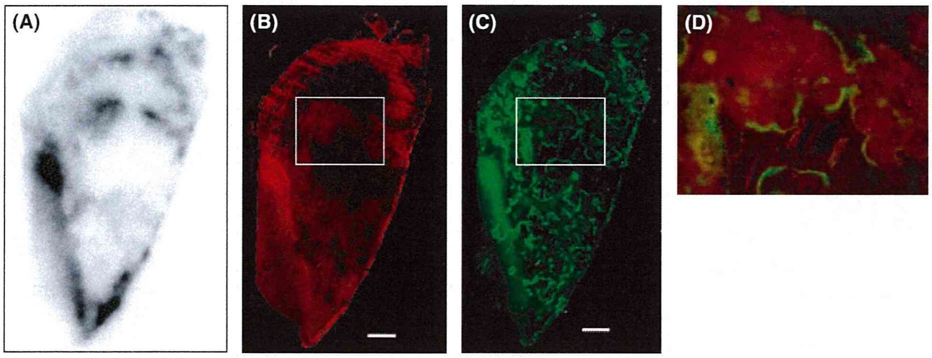

Fig. 3. Representative images of an autoradiogram (A), hypoxia-inducible factor (HIF)-1α immunostaining (B), and pimonidazole immunostaining (C) in the identical section. A high-magnification merged image of HIF-1α immunostaining with pimonidazole immunostaining (D, from insets in B,C) shows that some regions were positive for both stains (yellow) but others did not overlap (red or green). Bars = 1 mm (B,C).

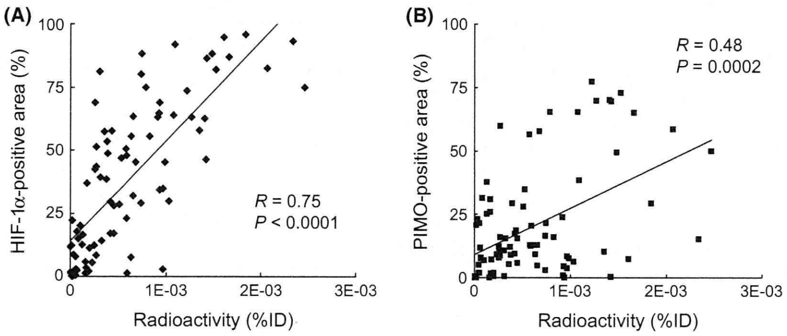

Fig. 4. Correlation between the intratumoral distribution of [^{125}I]IPOS and the level of hypoxia-inducible factor (HIF)-1α expression (A) or that of pimonidazole (PIMO)-adduct formation (B). The ordinate represents the percentage of HIF-1α- and PIMO-positive areas in each region of interest (ROI), and the abscissa represents [^{125}I]IPOS accumulation (%ID) in the same ROI. A total of 10 sections (two sections per tumor) were analyzed. Regression analysis of the areas showing [^{125}I]IPOS accumulation with HIF-1α- or PIMO-positive areas reveal a significantly positive correlation in both cases (HIF-1α: $R = 0.75$, $P < 0.0001$; PIMO: $R = 0.48$, $P = 0.0002$). The results of the chi-square-test reveal that the correlation coefficient between [^{125}I]IPOS and HIF-1α was significantly higher than that between [^{125}I]IPOS and PIMO ($P < 0.01$).

performance due to difficulties in attenuation and scattering correction, and the sensitivity of multi-pinhole SPECT is still lower than PET. However, because SPECT can theoretically achieve a higher spatial resolution than PET, wherein the resolution is limited by the positron range, it is suitable for small animal imaging. In fact, several multi-pinhole SPECT systems are able to image small components within mouse organs.(31,32) The *in vivo* images obtained in the present study were consistent with the results of *ex vivo* biodistribution. The tumor was clearly visualized, but no accumulation of radioactivity was observed in the opposite leg (Fig. 1A,B,D), indicating a high tumor/muscle ratio (10 in *ex vivo* biodistribution). Our observation of high radioactivity in the bladder (Fig. 1E) was in accordance with the finding that the radioactivity was mainly excreted in urine after the administration of [^{125}I]IPOS.

The characterization of [^{125}I]IPOS has been reported in a previous study.(14) Although the tumor uptake of [^{125}I]IPOS was significantly and positively correlated with HIF-1 transcriptional activity, suggesting the feasibility of [^{125}I]IPOS as an HIF-1-active tumor imaging probe, a direct comparison between the intratumoral distribution of [^{125}I]IPOS and HIF-1 expression has not yet been carried out. In the present study, the majority of the [^{125}I]IPOS-distributed areas in the tumor corresponded to HIF-1α-positive hypoxic areas, although there were a few unmatched regions (Fig. 3). A significant positive correlation was observed between the areas, and the correlation coefficient between [^{125}I]IPOS and HIF-1α was significantly greater than that between [^{125}I]IPOS and PIMO (Fig. 4). Although we cannot exclude the effect of the difference in the molecular sizes of [^{125}I]IPOS and PIMO on the distribution, these findings are consistent with the results of recent studies showing that HIF-1α-positive areas are not always colocalized with PIMO-positive areas.(33–35) Thus, [^{125}I]IPOS can be viewed as a probe that depicts HIF-1-active areas rather than the physically hypoxic areas themselves.

Although the detailed mechanism of cellular uptake and retention of [^{125}I]IPOS is now under investigation, we found that low temperature (4°C) or ATP depletion inhibited the cellular uptake of [^{125}I]IPOS (unpublished data). As most studies have shown endocytosis as the major cellular uptake pathway for most PTDs(36,37) and endocytosis occurs in an energy-dependent manner, [^{125}I]IPOS is probably uptaken by the cells through the endocytotic pathway. After uptake by endocytosis, [^{125}I]IPOS could be released from the endosomes and retained intracellularly because of its molecular size. In fact, in our previous experiment, [^{125}I]IPOS was not cleared from the cells under hypoxic conditions for at least 24 h, after the incubation medium was replaced with fresh medium.(14) Although the intracellular radioactivity decreased gradually under normoxic conditions, the cleared radioactivity was mainly attributable to the small molecules.(14) These findings indicated the intracellular retention ability of [^{125}I]IPOS.

doi: 10.1111/j.1349-7006.2011.02057.x